Magnetic structure and magnetization of helical antiferromagnets in high magnetic fields perpendicular to the helix axis at zero temperature

David C. Johnston

Phys. Rev. B **96**, 104405 — Published 5 September 2017

DOI: 10.1103/PhysRevB.96.104405

Magnetic Structure and Magnetization of Helical Antiferromagnets in High Magnetic Fields Perpendicular to the Helix Axis at Zero Temperature

David C. Johnston
Ames Laboratory and Department of Physics and Astronomy, Iowa State University, Ames, Iowa 50011
(Dated: August 14, 2017)

The zero-temperature angles of magnetic moments in a helix or sinusoidal fan confined to the xy plane, with respect to an in-plane magnetic field H_x applied perpendicular to the z axis of a helix or fan, are calculated for commensurate helices and fans with field-independent turn angles kd between moments in adjacent layers of the helix or fan using the classical J_0-J_1-J_2 Heisenberg model. For $0 < kd < 4\pi/9$, first-order transitions from helix to a fan structure occur at fields $H_{\rm t}$ as previously inferred, where the fan is found to be approximately sinusoidal. However, for $4\pi/9 \leq kd \leq \pi$, different behaviors are found depending on the value of kd and these properties vary nonmonotonically with kd. In this kd range, the change from helix to fanlike structure is usually a crossover with no phase transition between them, although first-order transitions are found for $kd = 3\pi/5$ and $8\pi/11$ and a second-order transition for $kd = 3\pi/4$. At a critical field $H_{\rm c}$, the fan or fanlike structures exhibit a second-order transition to the paramagnetic state. The $H_{\rm c}$ for a helix undergoing a field-induced change to a fan or fanlike structure is found to be the same as for a sinusoidal fan with the same kd and interlayer interactions. Analytical expressions for $H_{\rm c}$ versus kd are presented. We also calculated the average x-axis moment per spin $\mu_{x\rm ave}$ versus H_x for helices and fans with crossovers and phase transitions between them. When smooth helix to fanlike crossovers occur in the range $4\pi/9 \leq kd \leq \pi$, $\mu_{x\rm ave}$ exhibits an S-shape behavior with increasing H_x. This predicted behavior is consistent with $\mu_{x\rm ave}(H_x)$ data previously reported by Sangeetha, et al. [Phys. Rev. B **94**, 014422 (2016)] for single-crystal $EuCo_2P_2$ possessing a helix ground state with $kd \approx 0.85\pi$. The low-field magnetic susceptibility and the ratio $H_{\rm t}/H_{\rm c}$ are calculated analytically or numerically versus kd for helices, and are shown to approach the respective known limits for $kd \to 0$.

I. INTRODUCTION

The unified molecular field theory (MFT) for a spin lattice containing identical crystallographically-equivalent spins treats the magnetic and thermal properties of collinear and coplanar noncollinear Heisenberg antiferromagnets (AFMs) on the same footing [1–3]. This formulation has the added advantage that the theory is expressed in terms of readily measured quantities such as the spin S, the ordering temperature $T_{\rm N}$, the magnetic susceptibility χ at $T = 0$ and at $T_{\rm N}$, the Weiss temperature $\theta_{\rm p}$ in the Curie-Weiss law describing $\chi(T > T_{\rm N})$, and for a planar helix as shown in Fig. 1, the turn angle kd along the helix z axis between adjacent layers of ferromangetically (FM) aligned spins in zero magnetic field H. Here k is the wavevector of the helix along the z axis and d is the distance between adjacent layers of moments aligned ferromagnetically (FM) in the xy plane. The theory quantitatively describes the thermal and helical magnetic properties of $EuCo_2P_2$ single crystals, which is therefore considered to be a prototype for a helical AFM obeying the unified MFT [4]. The MFT was recently extended to include the influences of magnetic-dipole and uniaxial magnetocrystalline anisotropies on the thermal and magnetic properties of Heisenberg AFMs [5, 6].

In zero field the angle ϕ between the x axis and the FM-aligned moments within the xy plane in layer n is given by the linear relation

$$\phi_{n0} = n\,kd. \tag{1}$$

The above MFT was used to derive the anisotropic $\chi(T)$ and thermal properties of collinear and coplanar noncollinear AFMs in zero or low field at $T \leq T_{\rm N}$. In addition the average magnetic moment per spin $\mu_{z\rm ave}$ with high fields applied parallel to the helix z axis and the associated critical field were derived. However, in those studies the average magnetic moment $\mu_{x\rm ave}$ of a helical AFM structure versus high in-plane magnetic field H_x was not calculated.

Previous work on the influence of a large H_x on the classical magnetic structure of a helix at $T = 0$ indicated that with increasing H_x, the circular hodograph on the right side of Fig. 1 described by Eq. (1) first becomes distorted, and then a transition to a fan structure may occur at a field $H_{\rm t}$ in which the twofold rotational symmetry axis of the fan is aligned with the x axis [7–9]. It was also established that the wavevector of a helix changes when a large in-plane field is applied [7]. A numerical study of the phase diagram in the plane of the nearest- and next-nearest layer interactions J_1 and J_2, respectively (see Fig. 1), was carried out including the field-dependent helix or fan wavevector [10].

From analysis of the short-range order at finite temperature calculated by the transfer matrix method and zero-temperature calculations of the minimum energy of commensurate configurations, it was concluded that when the turn angle is in the range $0 < kd < \pi/2$, the helix to fan transition is first order, whereas for $\pi/2 < kd < \pi$ the change is continuous [11]. We find differences from this conclusion in both kd ranges. In particular, in the range $0 < kd < \pi/2$, for $kd = 4\pi/9$ we find a smooth crossover between the helix and fan phases with no phase transition. In the range $\pi/2 < kd < \pi$, in addition to smooth

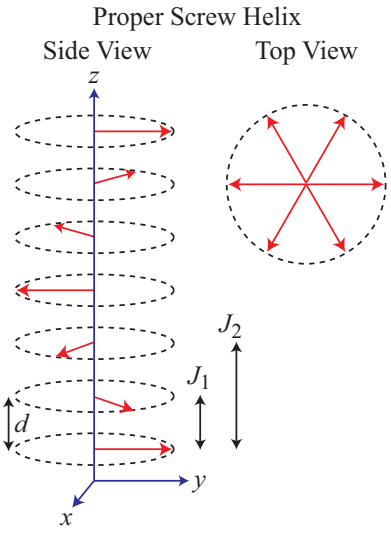

FIG. 1: (Color online) Generic helical AFM structure [1]. Each arrow represents a layer of moments perpendicular to the z axis that are ferromagnetically aligned within the xy plane and with interlayer separation d. The wave vector $\mathbf{k}$ of the helix is directed along the z axis. The magnetic moment turn angle between adjacent magnetic layers is kd. The nearest layer and next-nearest layer exchange interactions J_1 and J_2, respectively, within the J_0-J_1-J_2 Heisenberg MFT model are indicated.

crossovers with no phase transitions, we find first- and second-order transitions between the helix and fan phases for $kd = 8\pi/11$ and $kd = 3\pi/4$, respectively.

When a helix undergoes a transition to a sinusoidal fan structure in the xy plane in a high field H_x, perpendicular to the helix z axis, the angle ϕ_n of ordered moment $\vec{\mu}_n$ with respect to the positive x axis is

$$\phi_n = \phi_{\rm max} \sin(n\, kd), \tag{2}$$

where $\phi_{\rm max} > 0$ is the amplitude of the fan. We will show that under the assumption that the helix and fan wavevectors are the same and do not depend on the field, when the helix undergoes a first-order transition to a fan phase with increasing field, in general the fan phase is not sinusoidal, although the actual fan structure can be rather close to this structure depending on the value of the helix and fan wavevector. In addition we find many instances where the distorted helix instead undergoes a continuous evolution instead of a phase transition into a fan or fanlike structure.

Information about the helix and fan structures versus applied field at zero temperature has been provided for the continuum case in which $kd \to 0$ (almost ferromagnetic, see Fig. 1) [12]. In the helix structure in a field, the angle $\phi(z)$ of the xy-plane-oriented moments with respect to the positive x axis versus position along the helix z axis is given by the linear term (1) plus an approximately sinusoidal modulation described by [12]

$$\phi(z) = 2\pi\frac{z}{\lambda} - \frac{1}{5}\left(\frac{H_x}{H_c}\right)\sin\phi(z) \qquad \left(0 \le \frac{H_x}{H_c} \le 1/2\right), \tag{3}$$

where $H_{\rm c}$ is the critical field at which the x component of the moment reaches the saturation value. The value $H_{\rm t} = H_{\rm c}/2$ is the field at which the structure changes from helix to fan in a first-order transition. The result for $H_x/H_c = 1/2$ for maximum modulation of the linear term versus z/λ is shown in Fig. 2(a). The slightly distorted sine-wave modulation is shown in Fig. 2(b), which has an amplitude of only 1.6% of 2π. For the fan phase, the $\phi(z)$ is given by

$$\phi(z) = \phi_{\rm max}\sin(2\pi z/\lambda) \quad (1/2 \le H_x/H_{\rm c} \le 1), \tag{4a}$$

where the amplitude $\phi_{\rm max}$ of the sinusoidal fan is

$$\phi_{\rm max} = \frac{4}{3}\left[\left(\frac{H_{\rm c}}{H_x}\right)^{1/2} - 1\right] \quad \left(\frac{1}{2} \le \frac{H_x}{H_{\rm c}} \le 1\right). \tag{4b}$$

A plot of ϕ/π versus z/λ for $H_x/H_c = 1/2$ for the fan phase is shown in Fig. 2(c).

The transition from the distorted helix phase with the moment angle in Eq. (3) and Figs. 2(a) and 2(b) to that of the fan in Eqs. (4) and Fig. 2(c) is qualitatively similar to the transition from a periodically-modulated linear behavior to oscillating behavior for the simple pendulum with decreasing kinetic energy of the pendulum bob [13, 14].

In the above studies, the magnetic phase diagram at temperature $T = 0$ showing the regions of stability of the helix and fan phases within the exchange-interaction parameter space was of primary interest, with very few presentations of magnetization versus field data. Here we significantly extend these studies to provide a detailed comprehensive study of the $\phi_n(H_x)$ and $\mu_{x\rm ave}(H_x)$ from $H_x = 0$ to $H_x = H_{\rm c}$ for a wide variety of discrete rational kd values where we assume that kd is not affected by the applied field. A planar anisotropy is assumed to be present that is strong enough that the ordered moments remain in the xy plane for the applied field ranges considered here.

For example, for the helix and fan structures in the continuum limit $kd \to 0$ discussed above that was studied in 1961 [12], the $\mu_{x\rm ave}(H_x)$ was not presented. However, this can be obtained by averaging $\cos[\phi(z/\lambda)]$ for that structure over one wavelength λ for each value of $H_x/H_{\rm c}$. Our result is shown for both the helix region $0 \le H_x/H_{\rm c} \le 1/2$ and the fan region $1/2 \le H_x/H_c \le 1$ in Fig. 3. For the helix phase, the magnetization is proportional to field with a susceptibility $(\mu_{x\rm ave}/\mu_{\rm sat})/(H_x/H_{\rm c}) = 1/10$. In the fan phase, $\mu_{x\rm ave}$ for $H_x/H_{\rm c} = 1/2$ is already near saturation and varies nonlinearly upon increasing $H_x/H_{\rm c}$ to the value of unity. A first-order transition in $\mu_{x\rm ave}(H_x)$ between the helix and fan phases occurs. The data in this figure are very

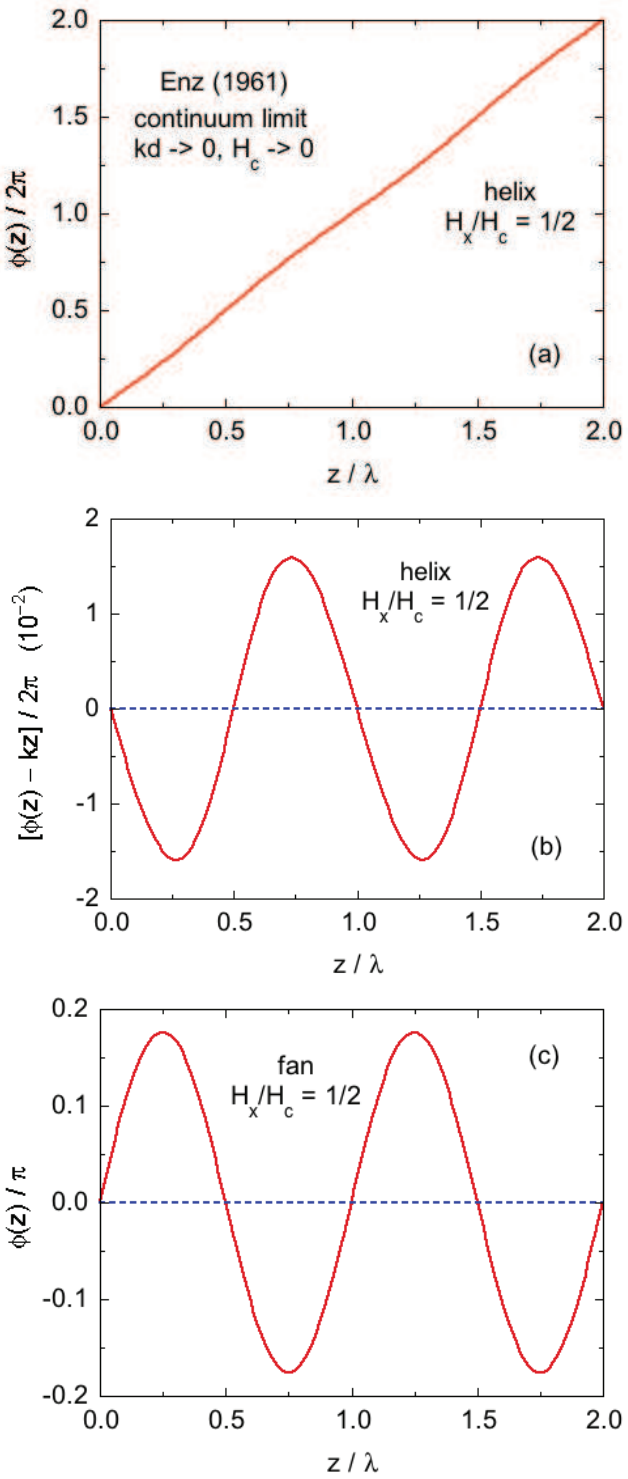

FIG. 2: (Color online) (a) Phase angle with respect to the $+x$ axis of the moments in planes at height z along a helix with an infintesimal angle kd between adjacent moment layers versus z/λ in an applied field $h_x/h_c = 1/2$, which is the boundary between the first-order transity with field between the helix and fan phases. (b) The near-sinusoidal modulation of the linear background kz phase of the helix in the field $h_x/h_c = 1/2$. (c) The phase ϕ of the moments in planes along the z axis in the fan structure versus z/λ with $h_x/h_c = 1/2$. These data were generated using the information in Ref. [12]

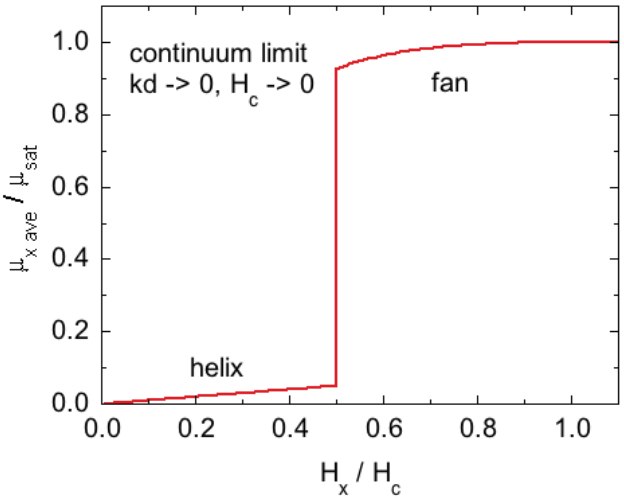

FIG. 3: (Color online) Our results for the reduced average moment $\mu_{x\mathrm{ave}}/\mu_{\mathrm{sat}}$ versus reduced field H_x/H_c for a helix or fan with an infinitesimal difference kd between the moment directions in adjacent moment layers. A first-order transition between the helix and fan structures occurs at $H_x/H_c = 1/2$ [12].

similar to those in Fig. 30 below for our smallest discrete value $kd = \pi/6$.

In addition to the intrinsic interest in the properties of helices and fans at high transverse fields, a primary motivation for the present work was to enable the high-field $\mu_{x\mathrm{ave}}(H_x)$ of real helix compounds at temperatures low compared with their T_{N} to be fitted by theory. $EuCo_2P_2$ has the $ThCr_2Si_2$ structure with space group $I4/mmm$, with the Eu^{+2} cations with spin $S = 7/2$ and spectroscopic splitting factor $g = 2$ occupying a body-centered tetragonal sublattice. Neutron diffraction measurements on a single crystal demonstrated AFM ordering of the Eu spins at $T_{\mathrm{N}} = 66.5(5)$ K with no contribution from the Co atoms [15]. The magnetic structure is a planar helix with the Eu ordered moments aligned in the ab plane of the tetragonal structure (xy plane here), with the helix axis along the perpendicular c axis (z axis here). The value of the AFM propagation vector corresponds to a turn angle kd between the ordered moments in adjacent layers of the helix at low temperatures given by

$$kd\,(15\ \mathrm{K}) = 0.852(4)\pi. \qquad (5)$$

This value of kd with $\pi/2 < kd < \pi$ indicates that the dominant *interlayer* interactions are AFM [1, 2], and dominant ferromagnetic (FM) *intralayer* interactions are then inferred from $\chi(T)$ measurements [4].

A detailed study of the magnetic and thermal properties of $EuCo_2P_2$ single crystals was carried out recently [4]. The low-field χ_{ab} below T_{N} was analyzed in terms of the above unified MFT and this theory was found [4] to accurately fit the data with a kd value similar to the neutron result in Eq. (5). However, the high-field $M_{ab}(H_{ab})$

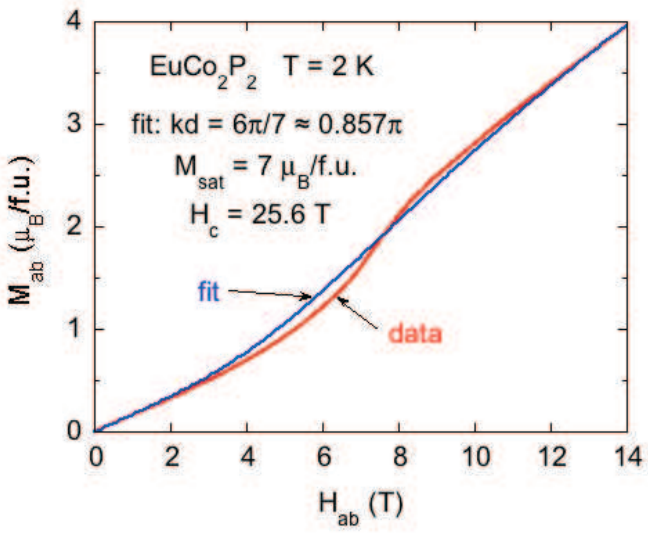

FIG. 4: (Color online) Magnetization M_{ab} versus transverse applied ab-plane magnetic field H_{ab} at a temperature of 2 K for tetragonal $EuCo_2P_2$ with a zero-field c-axis helical magnetic structure (red data) [4]. The fit to the data by the $M_{xy}(H_{xy})$ prediction for a helix with turn angle $6\pi/7$ with saturation magnetization $M_{\rm sat} = 7\ \mu_{\rm B}$/f.u. and critical field $H_c = 25.6$ T is shown as the blue curve.

data, shown in Fig. 4 [4], did not agree with the conventional wisdom that instead of an S-shaped metamagnetic feature as seen in the data, a first-order transition should occur with a distinct discontinuity in $M_{ab}(H_{ab})$ at a transition field $H_{\rm t} < H_{\rm c}$, as in Fig. 3.

This conundrum called for new calculations of the high-field $\mu_{x\rm ave}(H_x)$ for the helix. Our calculations provide clear predictions for comparison with experiment. They are also a benchmark for comparing the magnetic structures and magnetization versus field data within this model with the properties of more complicated systems such as helices and fans with a field-dependent kd and/or including quantum and/or additional anisotropy effects to see what changes these additional features create in the results. As a preview of our results, shown in Fig. 4 is a fit to the $M_{ab}(H_{ab})$ data for $EuCo_2P_2$ by our theoretical prediction with $kd = 0.86\pi$, close to the value in Eq. (5), which semiquantatively reproduces the S shape of the data at the observed field.

Section II gives an outline of the general theory we use to calculate the field dependences of the moment angles and in-plane magnetization versus applied in-plane field for the helix and sinusoidal fan. We assume for simplicity that the turn angle kd is independent of in-plane field and that the helix and fan are commensurate with the spin lattice as noted above. In order to calculate the magnetization versus field for a helix or fan, it is necessary that the number of moment layers per wavelength be an integer, which in turn requires that the wave vector be commensurate with the spin lattice. However, from calculations on commensurate helices/fans, we obtain results such as in Eq. (13c) and Fig. 5 and in Eqs. (21) below that we infer also apply to incommensurate wave vectors. The results for the dependences of the moment angles and magnetization of a sinusoidal fan structure are presented in Sec. III. Here we first discuss their dependences on kd and the ratio $J_{12} \equiv J_1/J_2$. Then we specialize to the cases where J_{12} takes the value associated with a helix with the same kd. This allows direct comparison of the sinusoidal fan properties with the high-field fan phase of the helix. This is of special interest because the moment angles in the field-induced fan originating from the helix are solved independently rather than enforcing a sinusoidal fan relationship on those angles. Therefore the field-induced fan may not be sinusoidal and hence a comparison of the moment angles in that fan and the magnetization with the corresponding properties of a strictly sinusoidal fan is of significant interest. The moment angles in the helix and the transverse magnetization versus transverse field are derived for specific values of kd in Sec. IV. We find that for $4\pi/9 \le kd \le \pi$, the evolution of the moment angles with increasing field from a distored helix to a fan or fanlike structure with increasing kd can be either a crossover, a second-order transition, or a first-order transition with no obvious dependence of their order versus kd. For this reason, plots of the phase angles and magnetization versus applied field are given for many kd values. A summary of our results on helices with field-independent wavevector (that may transition to fans with the same wavevector) is given in Sec. V, where a phase diagram is constructed versus kd.

II. THEORY

In this paper we use the one-dimensional J_0-J_1-J_2 model [1, 2] for both the helix and fan phases, where J_0 is the sum of the Heisenberg exchange interactions between a representative spin and the other spins in the same xy layer, J_1 is the sum of the interactions between the spin in one layer and the spins in either of the two nearest-neighbor layers along the z axis, and J_2 is the sum of the interactions of the spin with the spins in either of the two next-nearest neighbor layers, as shown in Fig. 1. In this model, the energy E_n of a spin S with ordered moment $\vec{\mu}_n$ consists of the sum of the exchange and Zeeman terms, given in general by [2]

$$E_n = \frac{S}{2}\Big\{SJ_0 + 2SJ_1\big[\cos(\phi_{n+1}-\phi_n) + \cos(\phi_{n-1}-\phi_n)\big] + 2SJ_2\big[\cos(\phi_{n+2}-\phi_n) + \cos(\phi_{n-2}-\phi_n)\big]\Big\} - \mu_n H_x \cos\phi_n, \quad (6)$$

where S is the spin angular momentum of a moment in units of $\hbar$, the prefactor of 1/2 is present because the exchange interaction energy between a pair of spins is equally shared between them, and ϕ_i is the angle between moment i and the positive x axis. A positive (negative) J

is AFM (FM). All energies are normalized by (positive) SJ_2. Also, we define the variables

$$J_{02} \equiv \frac{SJ_0}{SJ_2} = \frac{J_0}{J_2}, \quad J_{12} \equiv \frac{J_1}{J_2}, \quad h_x = \frac{g\mu_{\rm B}H_x}{J_2}, \tag{7}$$

where $\mu_{\rm B}$ is the Bohr magneton. The magnitude μ_n of each spin n is

$$\mu_n = \mu_{\rm sat} = gS\mu_{\rm B}, \tag{8}$$

where $\mu_{\rm sat}$ is the saturation moment of a spin, Eq. (6) becomes

$$\begin{aligned}\frac{E_n}{SJ_2} &= \frac{1}{2}\Big\{J_{02} + 2J_{12}\big[\cos(\phi_{n+1}-\phi_n) \\ &+ \cos(\phi_{n-1}-\phi_n)\big] + 2\big[\cos(\phi_{n+2}-\phi_n) \\ &+ \cos(\phi_{n-2}-\phi_n)\big]\Big\} - h_x\cos\phi_n.\end{aligned} \tag{9a}$$

The average energy per spin is

$$\frac{E_{\rm ave}}{SJ_2} = \frac{1}{n_\lambda}\sum_{n=0}^{n_\lambda-1}\frac{E_n}{SJ_2}, \tag{9b}$$

where n_λ is the number of FM-aligned layers per helix or fan wavelength λ along the z axis.

For a sinusoidal fan structure, the only variable to solve for is the amplitude $\phi_{\rm max}(h_x, kd)$ which is obtained by minimizing the energy with respect to $\phi_{\rm max}$ for given values of h_x and kd. For a helix, the ground-state moment configuration is determined by minimizing $E_{\rm ave}$ with respect to the n_λ values of ϕ_i in a helix for given values of h_x and kd. For both the fan and helix λ is assumed to be independent of h_x since kd is assumed to be. We will see that if a helical structure is assumed for low fields, a fan or fanlike structure, if they occur, is automatically generated with increasing h_x when solving for the $\phi_i(h_x)$ that minimize $E_{\rm ave}$. Thus we do not assume a sinusoidal fan structure *a priori* for a field-induced fan. Indeed, we find that the fan or fanlike structures obtained are never perfectly sinusoidal except near the reduced critical field $h_{\rm c}$. This observation is inferred from the fact that $h_{\rm c}$ for the field-induced fan or fanlike structure is identical to that for the sinusoidal fan calculated separately.

In the following two sections we apply the above general expressions first to the helix and then separately to the perfectly sinusoidal fan.

A. Helix Phases

In this paper we assume that a helix is commensurate with the spin lattice and that its wavelength $\lambda = n_\lambda d$ is independent of the applied field and contains n_λ layers, where d is the distance between FM-aligned moment layers along the z axis (see Fig. 1). The commensurate wave vector k of the helix is given in general by

$$k = \frac{2\pi m}{\lambda} = \frac{2\pi m}{n_\lambda d}, \tag{10}$$

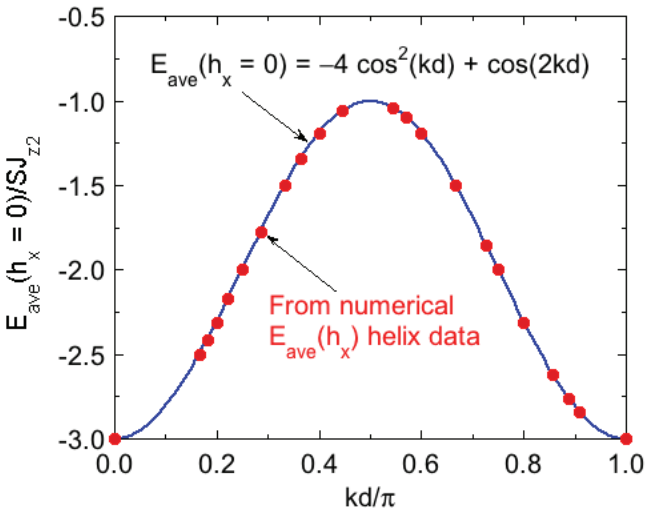

FIG. 5: (Color online) Average energy per spin $E_{\rm ave}$ normalized by SJ_2 in field $h_x = 0$ versus helix turn angle kd. The solid blue curve is the exact variation predicted in Eq. (13), whereas the red filled circles are from numerical calculations of $E_{\rm ave}(h_x)/SJ_2$ carried out later in Sec. IV.

where m is a positive integer and m/n_λ is an irreducible fraction. The reason that the variable integer m is included is because the helix or fan may be incommensurate for $m = 1$ but commensurate for $m > 1$ (see Table II below). Thus the magnitude of the turn angle between adjacent moment layers along the helix is

$$kd = \frac{2\pi m}{n_\lambda}, \tag{11}$$

where $2m/n_\lambda \le 1$ so that $kd \le \pi$. A kd satisfying $\pi < kd < 2\pi$ would correspond to a helix with $kd^* = 2\pi - kd$ that would have the opposite helicity but the same magnetization versus x-axis field response.

The phase differences in Eq. (9a) for a helix in zero field are

$$\phi_{n\pm1} - \phi_n = \pm kd, \qquad \phi_{n\pm2} - \phi_n = \pm 2kd. \tag{12}$$

Using the phase differences in Eq. (12), the energy per spin in Eq. (9a) becomes

$$\frac{E_n}{SJ_2} = \frac{1}{2}\left[J_{02} + 2J_{12}\cos(kd) + 2\cos(2kd)\right] - h_x\cos\phi_n. \tag{13a}$$

Minimizing the energy with respect to kd for $h_x = 0$ gives [2, 7]

$$J_{12} = -4\cos(kd) \qquad (h_x = 0), \tag{13b}$$

so Eq. (13a) becomes

$$\frac{E_n}{SJ_2} = \frac{1}{2}\left[J_{02} - 8\cos^2(kd) + 2\cos(2kd)\right] \qquad (h_x = 0). \tag{13c}$$

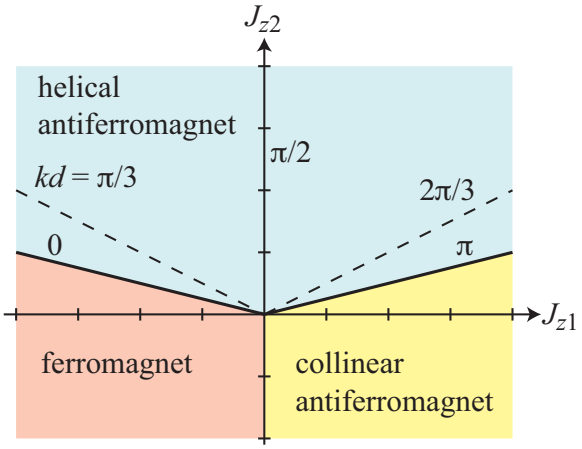

FIG. 6: (Color online) Zero-temperature phase diagram of the J_0-J_1-J_2 Heisenberg model [2]. The phase angle $\pi/2$ does not correspond to a helix because it would require $J_1 = 0$, resulting in two noninteracting AFM sublattices.

This variation is plotted as a solid blue curve in Fig. 5 after setting the reference energy $J_{02} = 0$. Also shown as red filled circles are the values abtained from numerical calculations of $E_{\rm ave}(h_x)$ discussed later in Sec. IV for which the kd values are listed in Table 5. The variation in Fig. 5 is symmetric about $kd = \pi/2$. Thus

$$E_{\rm ave}\left(h_x = 0, \frac{\pi}{2} - kd\right) = E_{\rm ave}\left(h_x = 0, \frac{\pi}{2} + kd\right). \quad (14)$$

This equality is seen to describe the particular pairs of discrete values $kd = 1/5,\ 4/5;\ 1/4,\ 3/4;\ 1/3,\ 2/3;$ and $2/5,\ 3/5$ for which we calculated $E_{\rm ave}(h_x)$. Thus for every helix with $0 \le kd < \pi/2$, there is another helix with $\pi/2 < kd \le \pi$ with the same energy at $h_x = 0$.

From Eq. (13b), the allowed domain of J_{12} for any helix within the present model is

$$0 < \left|J_{12}\right| \le 4, \quad (15)$$

where $J_2 > 0$ and J_{12} can be of either sign but $J_{12} = 0$ is excluded. The phase diagram in the J_1-J_2 plane at $T = H = 0$ for the J_0-J_1-J_2 model with $m = 1$ in Eq. (11) is shown in Fig. 6 [2]. The competing phases are the FM phase ($kd = 0$), the collinear A-type AFM phase ($kd = \pi$), and the helical phase ($0 < kd < \pi$). The value of the reduced exchange constant J_{02} in Eq. (13a) is irrelevant to the phase diagram.

We describe the angle ϕ_n of an ordered moment in an xy layer of a helix with respect to the positive x axis by

$$\begin{aligned} \phi_n &= n\,kd + \Delta\phi_n(h_x) \qquad (\text{odd } n_\lambda), \quad (16)\\ \phi_n &= \left(n + \frac{1}{2}\right) kd + \Delta\phi_n(h_x) \qquad (\text{even } n_\lambda), \end{aligned}$$

where $n = 0,\ 1,\ 2,\ \ldots,\ n_\lambda - 1$. The reason for the difference between these two equations is that for odd $n\lambda$, one moment is parallel to the field h_x and is unaffected by it, whereas for even $n\lambda$, one moment would also have to be antiparallel to the field and would not respond to the field because there would be no torque on it.

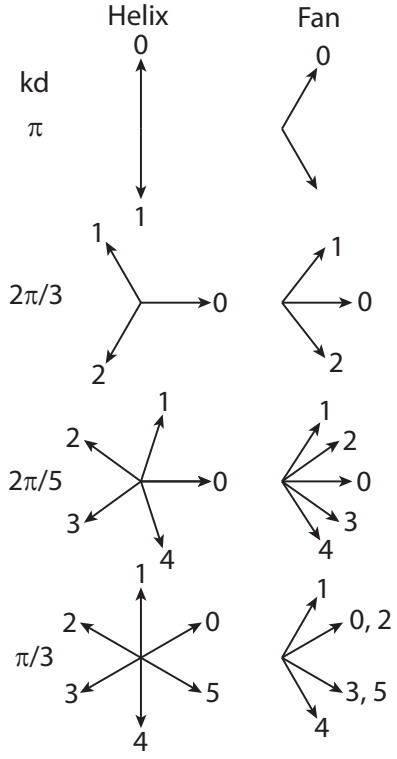

FIG. 7: (Color online) Illustration of the numbering of helix and fan moments in hodographs with different values of interlayer turn angle kd. The numbers are the subscripts n of the angles ϕ_n in Eqs. (16) and (18), respectively. Here we took $\phi_{\rm max}$ in Eq. (18) for a fan to be 60°. The $+x$ axis along which the transverse magnetic field is applied is directed towards the right and the z axis is pointed out of the page. However, for a helix changing to a field-induced fan with increasing field, the numbering of the moments in the helix is retained for all fields.

For either even or odd n_λ, the expressions for ϕ_n in Eqs. (16) give a symmetrical distribution of moments above and below the x axis in the xy plane, either with or without an applied field h_x, as shown for several helix examples in zero field in Fig. 7. That is, for every moment at angle $0 < \phi_n < \pi$ there is another moment at angle $-\phi_n$. This also holds in the presence of any x-axis field. Hence the number of $\Delta\phi_n(h_x)$ values to be solved for by minimizing the helix energy in Eq. (13c) at a given h_x is either $n_\lambda/2$ (for even n_λ) or $(n_\lambda - 1)/2$ (for odd n_λ). The multidimensional minimization of the energy to determine the unique values of $\Delta\phi_n$ with $\pi < \Delta\phi_n < 0$ was carried out using the `FindMinimum` utility of `Mathematica` for $3 \le n_\lambda \le 11$ (odd n_λ) or $2 \le n_\lambda \le 12$ (even n_λ). Note: when a field-induced transition or continuous evolution from helix to fan occurs, we label the angles ϕ_n by the notation in Eq. (16) and not by the notation for fans in Eq. (18) below.

Once the angles $\phi_n(h_x)$ are determined, the reduced x-axis components μ_{nx} of the ordered moments $\vec{\mu}_n$ and the average x-axis moment per spin $\mu_{x\rm ave}$ are obtained for either the helix or fan as

$$\begin{aligned} \mu_{nx}/\mu_{\rm sat} &= \cos\phi_n, \\ \mu_{x\rm ave}/\mu_{\rm sat} &= \frac{1}{n_\lambda}\sum_{n=0}^{n_\lambda-1}\mu_{nx}. \end{aligned} \tag{17}$$

A helix is usually the stable phase at low fields with respect to a fan or fanlike phase. The only exceptions are for $kd = \pi/2$, for which a helix phase does not exist, and for $kd = \pi$ and $2\pi/3$ for which the helix and fan phases are identical if the values of $J_{12} = 4$ and 2 for the helix, respectively, are used in the formulas for the fan (see following section). The low-field susceptibility of the helix $\chi_x \equiv \lim_{h_x\to 0}[\mu_{x\rm ave}(h_x)/\mu_{\rm sat}]/h_x$ can be obtained from the low-field $\mu_{x\rm ave}(h_x)/\mu_{\rm sat}$ magnetization versus field calculations. The more accurate method used here for a helix with a given value of kd is to express the average energy for the helix in Eq. (9a) in terms of the ϕ_n and h_x variables and then minimize the energy with respect to each of the ϕ_n with $0 < \phi_n < \pi$ which gives $n_\lambda/2$ (even n_λ) or $(n_\lambda - 1)/2$ (odd n_λ) equations. Each of these is Taylor expanded about $\phi_n = 0$ and $h_x = 0$ and only the first-order terms retained. Then the $n_\lambda/2$ or $(n_\lambda-1)/2$ linear equations are easily solved for the ϕ_n versus h_x using `Mathematica` and from those one obtains $\mu_{x\rm ave}$ to first order in h_x using Eqs. (17) from which χ_x can be obtained to arbitrary accuracy. In Table IV below, we quote χ_x to six figures and also include the exact analytic expressions for $\chi_x(kd)$ if obtained automatically by `Mathematica` using the above method.

B. Sinusoidal Fan Phases

At sufficiently high fields, the solutions for the $\phi_n(h_x)$ for a (distorted) helix structure change into values one may associate with a fanlike structure. This change can be either a continuous crossover, or a second-order transition for $4\pi/9 \lesssim kd \leq \pi$, or a first-order transition for $0 < kd \lesssim 4\pi/9$. However, because the ϕ_n values of the fanlike structure are determined from exact calculations for the helix (assuming that kd does not depend on field), it is not *a priori* clear that these solutions and the respective $\mu_{\rm ave}(h_x)$ values correspond precisely to those for a perfectly sinusoidal fan with a J_{12} of the helix with the same kd value as given in Eq. (13b). Therefore in this section we first discuss how to compute the $\phi_n(h_x)$ and $\mu_{x\rm ave}(h_x)$ of sinusoidal fans with arbitrary values of J_{12} and kd. Then we specialize to the values $J_{12} = -4\cos(kd)$ for comparison with the properties of the corresponding high-field fanlike phases of the helix with turn angle kd.

For a sinusoidal fan along the z axis with the moments aligned in the xy plane, the phase angle ϕ_n with respect to the $+x$ axis versus moment layer number n for a field-independent wavelength is defined as

$$\begin{aligned} \phi_n &= \phi_{\rm max}\sin(nkd) \qquad\qquad (\text{odd } n_\lambda), \\ \phi_n &= \phi_{\rm max}\sin\left[\left(n+\frac{1}{2}\right)kd\right] \quad (\text{even } n_\lambda), \\ & \qquad (n = 0,\ 1,\ \ldots, n_\lambda - 1), \end{aligned} \tag{18}$$

which differentiates between odd and even n_λ for the same reasons as in Eqs. (16), where the amplitude of the sinusoidal modulation of the phase is $0 \leq \phi_{\rm max} \leq \pi$ which is determined for general values of the parameters J_{12} and kd by minimizing the average energy per spin for each value of the reduced field h_x. The variations of ϕ_n with n for several fan examples are shown in Fig. 7.

The energy of moment n where kd is assumed independent of field is obtained from Eq. (9a) as

$$\frac{E_n}{SJ_2} = \frac{1}{2}\big[J_{02} + 2J_{12}\cos(kd) + 2\cos(2kd)\big] - h_x\cos\phi_n, \tag{19}$$

where the turn angle kd between adjacent moment layers along the z axis is given in Eq. (11), and the average energy per wavelength of the fan is given by Eq. (9b) in terms of the E_n values in Eq. (19). Thus for given values of J_{12}, kd, and h_x, the single remaining parameter $\phi_{\rm max}$ is found by minimizing $E_{\rm ave}$.

However, for $J_{12} = h_x = 0$, the values of $\phi_{\rm max}$ are determined by solving $\mu_{x\rm ave} = 0$ for $\phi_{\rm max}$ using Eqs. (17) (i.e., there is no net magnetization of the fan). The results are listed in Table I for $n_\lambda = 2\pi/kd$ values fom 2 to 23 for comparison with results below for nonzero J_{12} and h_x. One sees that the values asymptote rapidly to an $n_\lambda \to \infty$ limit given in the table caption. From Eq. (19), the average energies of all sinusoidal fans with $J_{12} = h_x = 0$ but different kd have the same value $J_{02}/2$.

III. FIELD-DEPENDENT RESULTS: SINUSOIDAL FAN PHASE

A. General Results

Values of $\phi_{\rm max}(h_x = 0)$ versus $kd = 2\pi m/n_\lambda$ were calculated for values of kd arising from the different combinations of m and n_λ in Eq. (11) listed in Table II. The critical field $h_{\rm c}$ was usually determined numerically from the criterion $h_{\rm c} = \lim_{\phi_{\rm max}\to 0}(h_x)$ using the `FindRoot` utility of `Mathematica`. The results in general depend on both J_{12} and h_x. We also find that physical solutions only exist for a range of J_{12} values that depend on the value of kd. For each value of kd, we found that $h_{\rm c}$ varies linearly with J_{12} over the physical range of J_{12} values listed in Table II. Exact analytic expressions are obtained for $\phi_{\rm max}$ and $h_{\rm c}$ versus J_{12} and h_x for $kd = \pi,\ 2\pi/3,\ \pi/2$, and $\pi/3$, as listed. Interestingly, the values of $\phi_{\rm max}(h_x = 0)$ for $kd = \pi,\ 2\pi/3$, and $\pi/2$ are seen to be identical with the corresponding values in Table I for $J_{12} = 0$ and $h_x = 0$.

TABLE I: Numerical values and/or analytic forms for the angular amplitude $\phi_{\max}$ for $J_{12} = h_x = 0$ versus number n_λ of moment layers per wavelength of the fan along the z axis with turn angle $kd = 2\pi/n_\lambda$. The values of $\phi_{\max}$ for both even and odd n_λ asymptote for large n_λ to the first zero of the zero-order Bessel function given by $j_{0,1} = 2.404\,825\,557\,695\,772\,768\,621\cdots$.

n_λ	$\phi_{\max}$ (rad)	n_λ	$\phi_{\max}$ (rad)
2	1.570 796 326 794 90	3	2.418 399 152 312 29
4	2.221 441 469 079 18	5	2.404 831 434 267 50
6	2.392 123 788 172 31	7	2.404 825 558 225 55
8	2.404 470 919 537 39	9	2.404 825 557 695 79
10	2.404 819 681 417 96	11	2.404 825 557 695 77
12	2.404 825 491 997 91	13	2.404 825 557 695 77
14	2.404 825 557 165 99	15	2.404 825 557 695 77
16	2.404 825 557 692 54	17	2.404 825 557 695 77
18	2.404 825 557 695 76	19	2.404 825 557 695 77
20	2.404 825 557 695 77	21	2.404 825 557 695 77
22	2.404 825 557 695 77	23	2.404 825 557 695 77
	Analytic Forms		
2	$\pi/2$		
3	$4\pi/3^{3/2}$		
4	$\pi/\sqrt{2}$		
6	$4\arctan\left(\sqrt{2\sqrt{3}-3}\right)$		

For some values of kd, only FM-polarized solutions of $\mu_{x\mathrm{ave}}(h_x = 0)$ are obtained. This is not relevant to cases where a helix with the given kd transitions to a fan with the same kd and J_{12} at finite h_x, at which a finite magnetization of the fan would naturally occur. The lower limit of a J_{12} range corresponds to the value at which the critical field $h_c \to 0$, whereas the upper limit (if present) is the maximum value at which a FM value of $\mu_{x\mathrm{ave}} \to 0$ (PM state), above which the FM value of $\mu_{x\mathrm{ave}}$ at $h_x = 0$ would become negative. In the last column of Table II is the J_{12} value of a helix with the same value of kd as for the fan according to Eq. (13b). One sees that for each value of kd, the helix value of J_{12} lies within the physical range of J_{12} for the fan. We have verified that within the physical range of J_{12}, the derived values of $\phi_{\max}$ correspond to minima (rather than maxima) of the energy. Once $\phi_{\max}(h_x,\ J_{12})$ is determined, the magnetization isotherms $\mu_{x\mathrm{ave}}/\mu_{\mathrm{sat}}$ versus h_x at $T = 0$ can be generated for different values of J_{12} within the physical range using Eqs. (17) and (18).

To illustrate sinusoidal fan structures and magnetizations, we present some representative plots of them. Shown in Fig. 8 are plots of $\phi_{\max}/\pi$, the angles ϕ_n/π of moments n with $0 \le \phi_n \le \pi$, and the average x-axis moment per spin $\mu_{x\mathrm{ave}}$ versus the reduced field h_x/h_c for (a) $kd = \pi$, $n_\lambda = 2$, (b) $kd = 2\pi/3$, $n_\lambda = 3$, and (c) $kd = \pi/2$, $n_\lambda = 4$. The indices n of the ϕ_n are the same as in, and dictated by, Eq. (18), examples of which

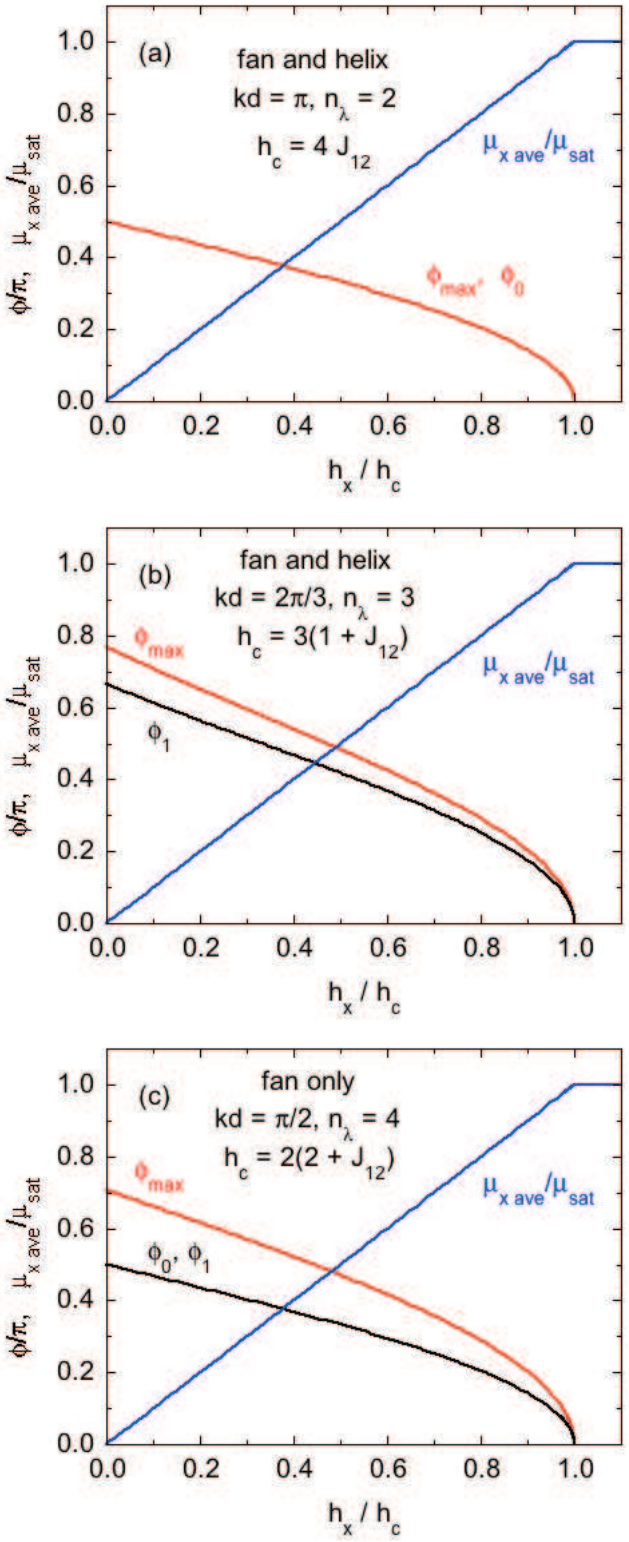

FIG. 8: (Color online) The amplitude $\phi_{\max}$ of the sinusoidal fan and the moment angles ϕ_n with $0 \le \phi_n \le \pi$ with respect to the $+x$ axis, both normalized by π rad, and the normalized average x-axis moment component per spin $\mu_{x_{\mathrm{ave}}}/\mu_{\mathrm{sat}}$ versus reduced x-axis field h_x/h_c for fans with turn angles kd given by (a) $kd = \pi$, (b) $kd = 2\pi/3$, and (c) $kd = \pi/2$. The subscripts n in ϕ_n are defined in Eqs. (18). The fan properties in (a) and (b) with the kd and J_{12} values of the respective helices are identical with those of the helices. The parameters of the fan in (c) have no helix counterpart, as explained in the text.

TABLE II: The dependence on kd and J_{12} of the amplitude $\phi_{\rm max}$ of the sinusoidal fan, the reduced critical field $h_{\rm c}$, and the physically-allowed range of the parameter J_{12} for the fan are listed for specific values of kd and n_λ, all determined by minimizing the energy of the fan. In the allowed fan J_{12} range, a minimum value corresponds to the value at which $h_{\rm c} = 0$, and the maximum value to the value at which a ferromagnetic $\mu_{x{\rm ave}}$ in $h_x = 0$ goes to zero. For $kd = 6\pi/11,\ 4\pi/7$, and $3\pi/5$, only FM solutions are found. Shown in the last column is the value of J_{12} of a helix with the same value of kd. A positive (negative) value of $J_{12} \equiv J_1/J_2$ corresponds to an AFM (FM) value of the nearest-layer exchange J_1.

kd	n_λ	$\phi_{\rm max}(h_x = 0)$	$\phi_{\rm max}(h_x, J_{12})$	$h_{\rm c}$	Physical Fan J_{12} Range	J_{12} for Helix
π	2	$\pi/2$	$\arccos(h_x/4J_{12})$	$4J_{12}$	$J_{12} \geq 0$	4
$10\pi/11$	11	depends on J_{12}	depends on J_{12}	$0.3179 + 3.9191J_{12}$	$J_{12} \geq 0.5213$	3.83797
$8\pi/9$	11	depends on J_{12}	depends on J_{12}	$0.4685 + 3.8793J_{12}$	$J_{12} \geq 0.6956$	3.75877
$6\pi/7$	7	depends on J_{12}	depends on J_{12}	$0.7534 + 3.8020J_{12}$	$J_{12} \geq 0.9160$	3.60388
$5\pi/6$	12	depends on J_{12}	depends on J_{12}	$1.0005 + 3.7321J_{12}$	$J_{12} \geq 1.0050$	3.46410
$4\pi/5$	5	depends on J_{12}	depends on J_{12}	$1.3823 + 3.6182J_{12}$	$J_{12} \geq 1$	3.23607
$3\pi/4$	8	depends on J_{12}	depends on J_{12}	$2.0005 + 3.4142J_{12}$	$J_{12} \geq 0.5858$	2.82843
$8\pi/11$	11	depends on J_{12}	depends on J_{12}	$2.2851 + 3.3098J_{12}$	$J_{12} \geq 0.3441$	2.61944
$2\pi/3$	3	$4\pi/3^{3/2}$	$\frac{2}{\sqrt{3}}\arccos\left[\frac{h_x-(1+J_{12})}{2(1+J_{12})}\right]$	$3(1 + J_{12})$	$J_{12} \geq -1$	2
$3\pi/5$	10	depends on J_{12}	depends on J_{12}	$3.6186 + 2.6178J_{12}$	$J_{12} \geq -1.3823$ (FM)	1.23607
$4\pi/7$	7	depends on J_{12}	depends on J_{12}	$3.8024 + 2.4451J_{12}$	$J_{12} \geq -1.5551$ (FM)	0.890084
$6\pi/11$	11	depends on J_{12}	depends on J_{12}	$3.9195 + 2.2846J_{12}$	$J_{12} \geq -1.7156$ (FM)	0.569259
$\pi/2$	4	$\pi/\sqrt{2}$	$\sqrt{2}\arccos\left[\frac{h_x}{2(2+J_{12})}\right]$	$2(2 + J_{12})$	$J_{12} \geq -2$	0
$2\pi/5$	5	depends on J_{12}	depends on J_{12}	$3.6186 + 1.3819J_{12}$	$-2.6185 \leq J_{12} \leq 1$	-1.23607
$4\pi/11$	11	depends on J_{12}	depends on J_{12}	$3.3095 + 1.1687J_{12}$	$-2.8317 \leq J_{12} \leq 0.6980$	-1.66166
$\pi/3$	6	$2\arccos\left(\frac{3-J_{12}}{6}\right)$	$2\arccos\left(\frac{3-J_{12}+h_x}{6}\right)$	$3 + J_{12}$	$-3 \leq J_{12} \leq 3(2-\sqrt{3})$	-2
	(6)				$-3 \leq J_{12} \leq 0.803848$	
$2\pi/7$	7	depends on J_{12}	depends on J_{12}	$2.4455 + 0.7530J_{12}$	$-3.2477 \leq J_{12} \leq -0.0917$	-2.49396
$\pi/4$	8	depends on J_{12}	depends on J_{12}	$2.0005 + 0.5858J_{12}$	$-3.4151 \leq J_{12} \leq -0.5858$	-2.82843
$2\pi/9$	9	depends on J_{12}	depends on J_{12}	$1.6532 + 0.4679J_{12}$	$-3.5332 \leq J_{12} \leq -0.9961$	-3.06418
$\pi/5$	10	depends on J_{12}	depends on J_{12}	$1.3826 + 0.3820J_{12}$	$-3.6197 \leq J_{12} \leq -1.3706$	-3.23607
$2\pi/11$	11	depends on J_{12}	depends on J_{12}	$1.1697 + 0.3175J_{12}$	$-3.6840 \leq J_{12} \leq -1.6933$	-3.36501
$\pi/6$	12	depends on J_{12}	depends on J_{12}	$1.0007 + 0.2680J_{12}$	$-3.7338 \leq J_{12} \leq -1.9689$	-3.46410
$2\pi/13$	13	depends on J_{12}	depends on J_{12}	$0.8643 + 0.2291J_{12}$	$-3.7732 \leq J_{12} \leq -2.2036$	-3.54182
$\pi/7$	14	depends on J_{12}	depends on J_{12}	$0.7537 + 0.1981J_{12}$	$-3.8043 \leq J_{12} \leq -2.4037$	-3.60388
$2\pi/15$	15	depends on J_{12}	depends on J_{12}	$0.6623 + 0.1729J_{12}$	$-3.8299 \leq J_{12} \leq -2.5748$	-3.65418
$\pi/8$	16	depends on J_{12}	depends on J_{12}	$0.5863 + 0.1523J_{12}$	$-3.8510 \leq J_{12} \leq -2.7215$	-3.69552
$2\pi/17$	17	depends on J_{12}	depends on J_{12}	$0.5225 + 0.1351J_{12}$	$-3.8685 \leq J_{12} \leq -2.8480$	-3.72989
$\pi/9$	18	depends on J_{12}	depends on J_{12}	$0.4684 + 0.1206J_{12}$	$-3.8835 \leq J_{12} \leq -2.9576$	-3.75877
$2\pi/19$	19	depends on J_{12}	depends on J_{12}	$0.4221 + 0.1083J_{12}$	$-3.8963 \leq J_{12} \leq -3.0528$	-3.78327
$\pi/10$	20	depends on J_{12}	depends on J_{12}	$0.3825 + 0.0979J_{12}$	$-3.9073 \leq J_{12} \leq -3.1361$	-3.80423
$2\pi/21$	21	depends on J_{12}	depends on J_{12}	$0.3479 + 0.0888J_{12}$	$-3.9171 \leq J_{12} \leq -3.2093$	-3.82229
$\pi/11$	22	depends on J_{12}	depends on J_{12}	$0.3179 + 0.0810J_{12}$	$-3.9251 \leq J_{12} \leq -3.2738$	-3.83797
$2\pi/23$	23	depends on J_{12}	depends on J_{12}	$0.2915 + 0.0741J_{12}$	$-3.9327 \leq J_{12} \leq -3.3309$	-3.85167
0	∞					-4

are shown in Fig. 7. In all plots such as these shown in this paper, there exist moment angles that are the negatives of the ones shown at each h_x (see Fig. 7). The $\mu_{x{\rm ave}}$ is seen to be proportional to h_x for each set of parameters shown. This is a general characteristic of the sinusoidal fan phase.

The plots in Figs. 8(a)–8(c) are valid for all J_{12} values within the physical ranges listed in Table II for the given sets of parameters. The dependences on J_{12} are taken into account via the normalization of the horizontal axes by the J_{12}-dependent critical fields $h_{\rm c}$. We also emphasize that the behaviors in Figs. 8(a) and 8(b) are found to be identical with those of helices with the same special parameters and hence exhibit no phase transitions versus field other than that at the reduced critical field $h_{\rm c}$. The fan in Fig. 8(c) with a turn angle of $kd = \pi/2$ has no helix

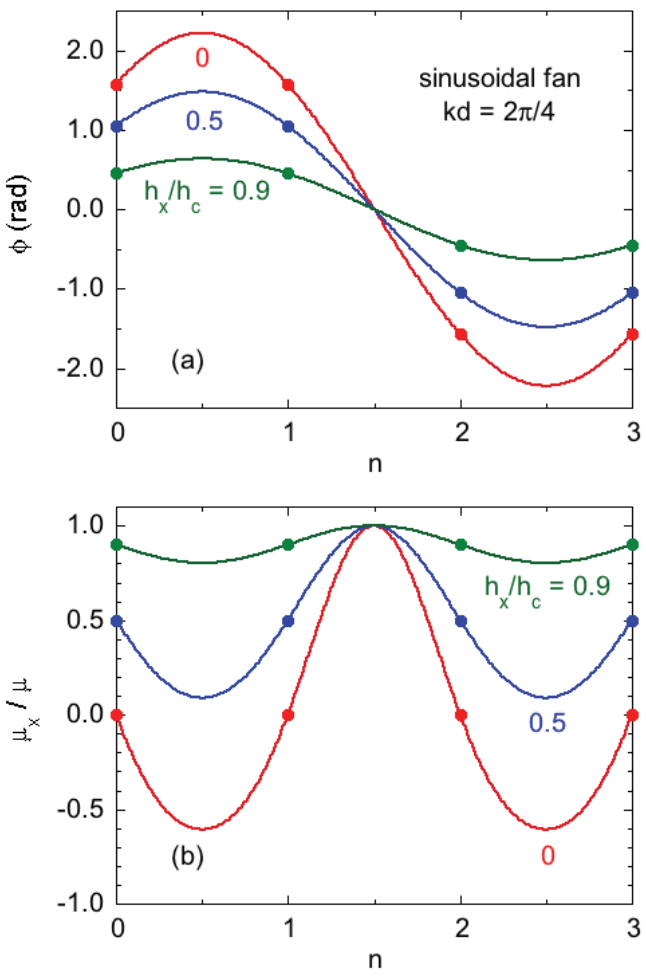

FIG. 9: (Color online) Plots of (a) ϕ_n and (b) μ_x versus n for $kd = \pi/2$ with $n_\lambda = 4$ for three values of the reduced field h_x/h_c, showing that the physical moments with integer n lie on sinusoids described by Eq. (18).

counterpart, because according to Eq. (13b) that would require that $J_{1z} = 0$ which would result in two noninteracting sets of next-nearest-neighbor collinear AFM layers, each with a response to a field given by the behavior for $kd = \pi$ in Fig. 8(a). Shown in Fig. 9 are plots of ϕ_n versus n for $kd = \pi/2$ with $n_\lambda = 4$, which show that even though the fan is sinusoidal the actual angles for the moments may not appear to be so.

In the fan phases appearing above the transition field h_t of a helix, the values of ϕ_n are not *a priori* prescribed as in Eq. (18) for the sinusoidal fan. Instead, the set of ϕ_n for a given kd is found by multidimensional minimization of the energy with the ϕ_n as independent variables as discussed previously and could therefore be nonsinusoidal. Indeed, we infer that the fan structure of the helices above h_t obtained by energy minimization is indeed sinusoidal for $h_x \to h_c$, since h_c for the field-induced fan is found to be identical to that of the sinusoidal fan by itself. However, at smaller h_x values in the fan phase, deviations from the predictions of the moment angles for sinusoidal fans are found as illustrated in Sec. IV below.

B. Fans with Helix J_{12} Values

Helix structures can undergo a transition from the helix phase to a fan phase at sufficiently large reduced fields h_x [7]. Therefore, a particularly interesting case is when kd for the fan is the same as for a commensurate helix and when J_{12} is the same as given by Eq. (13b) for a helix with turn angle kd. Special cases of these equalities are illustrated in Figs. 8(a) and 8(b). Although in general the wavelength of a helix along the z axis depends on h_x, contrary to the assumption of this paper, when h_x approaches the critical field h_c, the wave vector of the fan is the same (kd) as for the corresponding helix in zero field [7]. This is consistent with our result that h_c for the sinusoidal fan is the same as that found from energy minimization of the helix in the field-induced fan regime, both with the same values of kd and J_{12}, as shown in the following Sec. IV.

Plots of the fan amplitudes $\phi_{\rm max}$, moment angles ϕ_n and reduced average x-axis moments $\mu_{x\rm ave}/\mu_{\rm sat}$ versus the reduced field ratio h_x/h_c for J_{12} values corresponding to helix turn angles $kd = 3\pi/4$, $3\pi/5$, $4\pi/11$, and $\pi/6$ are presented in Fig. 10. Two of these kd values are greater than $\pi/2$ (AFM J_1) and two are smaller (FM J_1) and were chosen to be representative of values for helices that show clear helix to fan transitions (either first or second order) in both ranges of kd as shown later. For $kd \gtrsim 4\pi/9$, we find that the helix-to-fanlike structure change is usually but not always a smooth crossover rather than a phase transition.

We obtain the reduced critical field h_c for the particular values $J_{12} = -4\cos(kd)$ of the sinusoidal fan as follows. The cosine terms in the average energy expression (9a) for E_n are expanded to fourth order in the arguments ϕ_n given in Eq. (18). Then the average energy $E_{\rm ave}$ in Eq. (9b) is minimized with respect to $\phi_{\rm max}$, yielding an expression for $\phi_{\rm max}$ in terms of kd, n_λ, and the reduced field h_x. The fan to PM phase transition occurs when $\phi_{\rm max} \to 0$. Solving for $h_x \equiv h_c$ in the expression $\phi_{\rm max}(kd, n_\lambda, h_x) = 0$ yields the following solutions for h_c in terms of kd and n_λ. The solutions for odd or even n_λ are

$$h_c = \frac{\rm Num(odd\ or\ even)}{\rm Denom(odd\ or\ even)}, \qquad (20a)$$

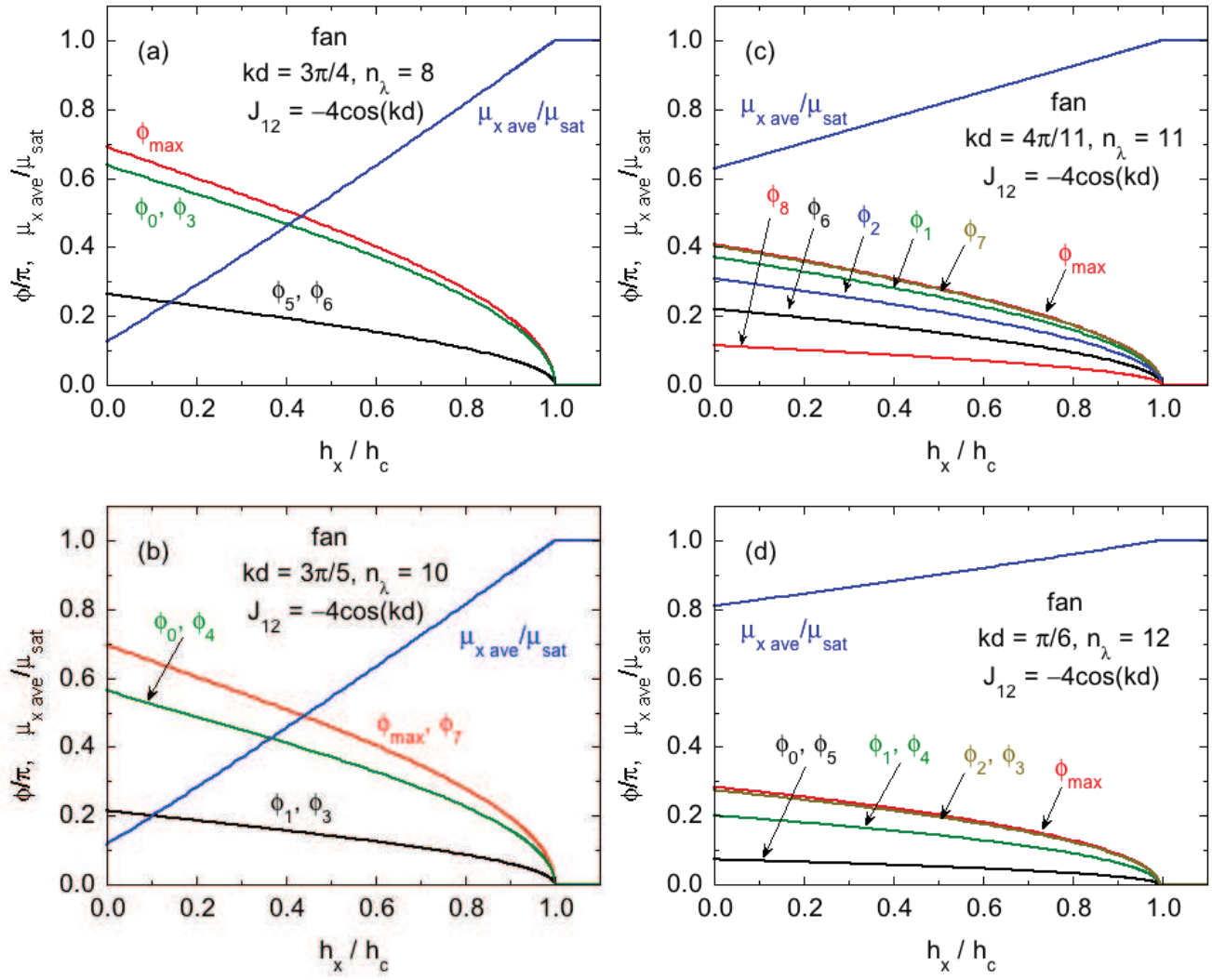

FIG. 10: (Color online) Plots as in Fig. 8 of sinusoidal fans with (a) $kd = 3\pi/4$, $n_\lambda = 8$, (b) $kd = 3\pi/5$, $n_\lambda = 10$, (c) $kd = 4\pi/11$, $n_\lambda = 11$, and (d) $kd = \pi/6$, $n_\lambda = 12$. For each kd the value of J_{12} must also be specified. These are chosen to be the values for the helices with the same kd values using Eq. (13b) as given in each figure. The sinusoidal fan properties are similar to those of helices with the same kd and J_{12} values above their respective helix to fan transition fields.

where

$$\begin{aligned}
\text{Num(odd)} &= 8\sin^4(kd/2)\Big\{-3+4n_\lambda+3\cos(2kd\,n_\lambda)+\csc(kd)\big\{-\sin(3kd)+\sin[kd(3-2n_\lambda)]\big\} \\
&\quad -2\big\{5\cos(kd\,n_\lambda)+\ 4\cos[kd(1-n_\lambda)]\big\}\cot(kd)\sin(kd\,n_\lambda)\Big\}, \\
\text{Denom(odd)} &= -1+2n_\lambda+\csc(kd)\sin[kd(1-2n_\lambda)]
\end{aligned} \tag{20b}$$

$$\begin{aligned}
\text{Num(even)} &= 8\sin^4(kd/2)\Big\{4n_\lambda\sin(kd)+\cos(2kd\,n_\lambda)\sin(2kd) \\
&\quad -[4+4\cos(kd)+\cos(2kd)]\sin(2kd\,n_\lambda)-\sin[2kd(1+n_\lambda)]\Big\}, \\
\text{Denom(even)} &= 2n_\lambda\sin(kd)-\sin(2kd\,n_\lambda)
\end{aligned} \tag{20c}$$

The critical fields h_c calculated from Eqs. (20) are listed for 72 values of kd in Table III with both even

TABLE III: Critical field h_c for second-order transitions of the fan to the paramagnetic phase using the J_{12} for the helix with the same turn angle kd obtained using Eq. (13b).

kd/π	kd/π	n_λ	h_c (helix J_{12})	h_c (helix J_{12})	kd/π	kd/π	n_λ	h_c (helix J_{12})	h_c (helix J_{12})
11/12	0.916667	24	$16\cos^4(\pi/24)$	1.54595e+01	5/12	0.416667	24	$16\sin^4(5\pi/24)$	2.19740e+00
10/11	0.909091	11	$16\cos^4(\pi/22)$	1.53585e+01	2/5	0.4	5	$5(3-\sqrt{5})/2$	1.90983e+00
9/10	0.9	20	$16\cos^4(\pi/20)$	1.52265e+01	8/21	0.380952	21	$16\sin^4(4\pi/21)$	1.61117e+00
8/9	0.888889	9	$16\cos^4(\pi/18)$	1.50496e+01	3/8	0.375	16	$16\sin^4(3\pi/16)$	1.52432e+00
7/8	0.875	16	$16\cos^4(\pi/16)$	1.48052e+01	4/11	0.363636	11	$16\sin^4(2\pi/11)$	1.36696e+00
6/7	0.857143	7	$16\cos^4(\pi/14)$	1.44547e+01	6/17	0.352941	17	$16\sin^4(3\pi/17)$	1.22882e+00
5/6	0.833333	12	$7+4\sqrt{3}$	1.39282e+01	8/23	0.347826	23	$16\sin^4(4\pi/23)$	1.16612e+00
9/11	0.818182	22	$16\cos^4(\pi/11)$	1.35609e+01	1/3	0.333333	6	1	1
4/5	0.8	5	$5(3+\sqrt{5})/2$	1.30902e+01	6/19	0.315789	19	$16\sin^4(3\pi/19)$	8.21024e−01
7/9	0.777778	18	$16\cos^4(\pi/9)$	1.24757e+01	4/13	0.307692	13	$16\sin^4(2\pi/13)$	7.46272e−01
10/13	0.769231	13	$16\cos^4(3\pi/26)$	1.22292e+01	3/10	0.3	20	$16\sin^4(3\pi/20)$	6.79684e−01
3/4	0.75	8	$2(3+2\sqrt{2})$	1.16569e+01	2/7	0.285714	7	$16\sin^4(\pi/7)$	5.67040e−01
8/11	0.727273	11	$16\cos^4(3\pi/22)$	1.09543e+01	3/11	0.272727	22	$16\sin^4(3\pi/22)$	4.76484e−01
5/7	0.714286	14	$16\cos^4(\pi/7)$	1.05429e+01	4/15	0.266667	15	$16\sin^4(2\pi/15)$	4.37898e−01
7/10	0.7	20	$16\cos^4(3\pi/20)$	1.00842e+01	6/23	0.260870	23	$16\sin^4(3\pi/23)$	4.03090e−01
2/3	0.666667	3	9	9	1/4	0.25	8	$2(3-2\sqrt{2})$	3.43146e−01
7/11	0.636364	22	$16\cos^4(2\pi/11)$	8.01360e+00	4/17	0.235294	17	$16\sin^4(2\pi/17)$	2.72465e−01
5/8	0.625	16	$16\cos^4(3\pi/16)$	7.64725e+00	2/9	0.222222	9	$16\sin^4(\pi/9)$	2.18941e−01
8/13	0.615385	13	$16\cos^4(5\pi/26)$	7.33982e+00	4/19	0.210526	19	$16\sin^4(2\pi/19)$	1.77847e−01
3/5	0.6	10	$(7+3\sqrt{5})/2$	6.85410e+00	1/5	0.2	10	$(7-3\sqrt{5})/2$	1.45898e−01
10/17	0.588235	17	$16\cos^4(7\pi/34)$	6.48887e+00	4/21	0.190476	21	$16\sin^4(2\pi/21)$	1.20772e−01
7/12	0.583333	24	$16\cos^4(5\pi/24)$	6.33850e+00	2/11	0.181818	11	$16\sin^4(\pi/11)$	1.00802e−01
4/7	0.571429	7	$16\cos^4(3\pi/14)$	5.97823e+00	4/23	0.173913	23	$16\sin^4(2\pi/23)$	8.47748e−02
5/9	0.555556	18	$16\cos^4(2\pi/9)$	5.50980e+00	1/6	0.166667	12	$7-4\sqrt{3}$	7.17968e−02
6/11	0.545455	11	$16\cos^4(5\pi/22)$	5.21953e+00	2/13	0.153846	13	$16\sin^4(\pi/13)$	5.24813e−02
8/15	0.533333	15	$16\cos^4(7\pi/30)$	4.87993e+00	1/7	0.142857	14	$16\sin^4(\pi/14)$	3.92287e−02
10/19	0.526316	19	$16\cos^4(9\pi/38)$	4.68791e+00	2/15	0.133333	15	$16\sin^4(\pi/15)$	2.98976e−02
1/2	1/2	4	4	4	1/8	0.125	16	$16\sin^4(\pi/16)$	2.31773e−02
10/21	0.476190	21	$16\sin^4(5\pi/21)$	3.42450e+00	2/17	0.117647	17	$16\sin^4(\pi/17)$	1.82400e−02
8/17	0.470588	17	$16\sin^4(4\pi/17)$	3.29591e+00	1/9	0.111111	18	$16\sin^4(\pi/18)$	1.45479e−02
6/13	0.461538	13	$16\sin^4(3\pi/13)$	3.09382e+00	2/19	0.105263	19	$16\sin^4(\pi/19)$	1.17431e−02
5/11	0.454545	22	$16\sin^4(5\pi/22)$	2.94250e+00	1/10	0.1	20	$16\sin^4(\pi/20)$	9.58186e−03
4/9	0.444444	9	$16\sin^4(2\pi/9)$	2.73143e+00	2/21	0.0952381	21	$16\sin^4(\pi/21)$	7.89510e−03
10/23	0.434783	23	$16\sin^4(5\pi/23)$	2.53793e+00	1/11	0.0909091	22	$16\sin^4(\pi/22)$	6.56328e−03
3/7	0.428571	14	$16\sin^4(3\pi/14)$	2.41789e+00	2/23	0.0869565	23	$16\sin^4(\pi/23)$	5.50051e−03
8/19	0.421053	19	$16\sin^4(4\pi/19)$	2.27717e+00	1/12	0.0833333	24	$16\sin^4(\pi/24)$	4.64420e−03

and odd $n_\lambda \le 24$. We infer that from the list of analytic h_c expressions for the discrete values in the ranges $0 < kd \le \pi/2$ and $\pi/2 \le kd \le \pi$ in Table III, h_c can respectively be expressed for all cases as

$$h_c = 16\sin^4\left(\frac{kd}{2}\right) \qquad (0 \le kd \le \pi/2), \tag{21a}$$

$$h_c = 16\cos^4\left(\frac{\pi - kd}{2}\right) \qquad (\pi/2 \le kd \le \pi). \tag{21b}$$

Since Eqs. (21) apply to all discrete values of kd in Table III, we suggest that the same formulae also apply to incommensurate (continuous) values of kd in the respective ranges. In the limit of small kd, Eq. (21a) gives

$$h_c = (kd)^4 \qquad (kd \to 0). \tag{22}$$

For such small values of kd, the system is nearly ferromagnetic (see Fig. 6). A result equivalent to Eq. (22) was obtained via a continuum model in Ref. [12].

Shown in Fig. 11(a) is a plot of h_c versus kd/π over the full range $0 \le kd/\pi \le 1$ according to the continuum

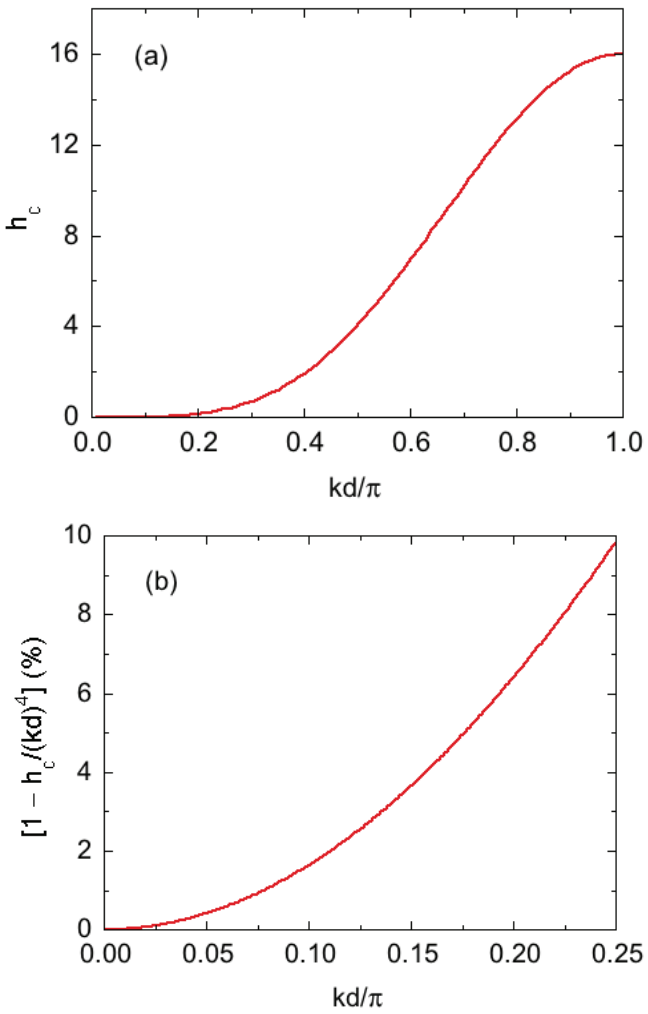

FIG. 11: (Color online) (a) The critical field h_c versus the turn angle kd between adjacent layers of a sinusoidal fan structure with J_{12} set to $J_{12} = -4\cos(kd)$ for helices, in units of π, for the range $0 < kd \leq 1$ described by Eqs. (21). (b) The percentage difference between h_c and the limiting behavior $(kd)^4$ for the region $0 < kd \leq 1/4$.

Eqs. (21). Figure 11(b) shows the percentage difference between h_c and the limiting behavior $(kd)^4$ for $kd \to 0$ in Eq. (22). For example, the h_c value for the smallest value $kd = \pi/12$ in Table III is about 1.13% larger than the limiting expression.

The dependence of $\phi_{\rm max}$ on h_x, kd and n_λ is determined by setting the derivative of the energy with respect to $\phi_{\rm max}$ to zero and solving for $\phi_{\rm max}$ from the resultant expression. For commensurate helices and fans, all possible kd values are written as

$$kd = \frac{2\pi m}{n_\lambda}, \tag{23}$$

where m and n_λ are positive integers with $2m \leq n_\lambda$ so that $kd \leq \pi$. Here we solve for the critical behavior of $\phi_{\rm max}(h_x)$ for h_x close to h_c by expanding the energy to fourth order in $\phi_{\rm max}$ and then setting the derivative of the energy with respect to $\phi_{\rm max}$ to zero. Solving the resultant expression for $\phi_{\rm max}$ yields

$$\phi^2_{\rm max}(h_x) = \frac{8\big[-6 + h_x + 8\cos(2\pi m/n_\lambda) - 2\cos(4\pi m/n_\lambda)\big]}{-22 + h_x + 28\cos(2\pi m/n_\lambda) - 8\cos(4\pi m/n_\lambda) + 4\cos(6\pi m/n_\lambda) - 2\cos(8\pi m/n_\lambda)} \quad (h_x \to h_c^-). \tag{24}$$

As anticipated in Ref. [7], the critical behavior obtained from Eq. (24) is mean-field-like as expected for the present classical treatment, with

$$\phi_{\rm max} = A(h_x)\left(1 - \frac{h_x}{h_c}\right)^{1/2} \qquad (h_x \to h_c^-), \tag{25a}$$

where the amplitude $A(h_x)$ in radians is given by

$$A(h_x) = \sqrt{\frac{4}{3 + 2\cos(kd) + \cos(2kd)}}. \tag{25b}$$

To plot the field dependence of $\phi_{\rm max}$ from these expressions, one needs to first insert the appropriate $h_c(m, n_\lambda)$ from Table III or Eqs. (21) into Eq. (25a).

For $kd \ll 1$ (close to the ferromagnetic limit, see

Fig. 6), a Taylor series expansion of Eq. (25b) to lowest order in kd gives

$$A(h_x) = \sqrt{\frac{2}{3}}\left[1 + \frac{(kd)^2}{4}\right] \quad (kd \ll 1). \tag{26}$$

For $m = 1$, keeping only the first term in the expansion and combining this with Eq. (25a) for $m = 1$ gives the small-kd continuum limit as

$$\phi_{\max} = \sqrt{\frac{2}{3}}\left(1 - \frac{h_x}{h_{\rm c}}\right)^{1/2} \quad (h_x \to h_{\rm c}^-,\ m = 1), \tag{27}$$

where h_c is given by Eq. (22).

IV. FIELD-DEPENDENT RESULTS: HELIX PHASES WITH CROSSOVERS OR TRANSITIONS TO FAN PHASES

In general, the helix phase competes with the fan phase in high fields [7]. However, in our treatment we minimize the energy of the helix with respect to all angles ϕ_n independently, so there is no specification in the minimization about whether the system is in the helix or fan phase at a particular value of h_x or in some sort of transition between them. One cannot avoid obtaining a fan phase if the energy minimization for a particular field gives a set of ϕ_n values corresponding to a fan, and correspondingly also for the helix phase. However, as already noted, a fan phase obtained this way does not have an exact sinusoidal fan configuration except in the limit $h_x \to h_{\rm c}$. This observation is explicitly illustrated later in Figs. 17, 18, 23, and 30. Irrespective of the differences between the fan moment angles and those of the sinusoidal fans, the average moment per spin versus field appear to be identical for each kd.

In the following two sections we discuss the structures and magnetizations versus transverse field of the two categories of helices with $J_1 > 0$ (AFM) and $J_1 < 0$ (FM) with $\pi/2 < kd \le \pi$ and $0 < kd < \pi/2$, respectively, according to Eq. (13b). Because we find that these properties vary nonmonotonically with kd, it is necessary to present the results for many kd values to illustrate the variety and evolution of the results. As part of these studies, we examined how the angles ϕ_n of the individual moments with respect to the $+x$ axis along which the field is aligned evolve with increasing field, as part of the energy minimization used to determine them. Therefore, the subscript n in ϕ_n refers to the helix convention in Eqs. (16) and Fig. 7 for all fields, even when the helix changes into a fan with increasing field.

A. $\pi/2 < kd \le \pi$: AFM $J_1 > 0$

Figures 12–20 show how the helix angles ϕ_n and the reduced average moment $\mu_{x\rm ave}/\mu_{\rm sat}$ per spin versus reduced field h_x change as kd is reduced from $10\pi/11$ to $6\pi/11$. The dominant behavior is a smooth crossover in the ordering of the ϕ_n angles from their initial helical values to a distribution approximating a sinusoidal fan for $h_x \to h_{\rm c}$. This smooth evoluation in $\phi_n(h_x)$ is accompanied by a smooth variation in $\mu_{x\rm ave}(h_x)$ as shown, which is not proportional to h_x but rather shows an S-shaped modulation of varying strength depending on kd that is strongest for $kd = 6\pi/7$ where a first-order transition almost occurs. We have previously shown a fit of the prediction for $kd = 4\pi/7$ in Fig. 14(b) to the measured magnetization data for $EuCo_2P_2$ in Fig. 4, which also shows an S-shaped behavior. The fit is not perfect in the S-shaped region, but it illustrates that a helix to fan transition in real materials need not be first order as often assumed previously but can be a smooth crossover instead, as suggested in Ref. [11].

Several kd values in the range $\pi/2 < kd \le \pi$ were found to show interesting variations in the properties different from smooth crossovers from helix to fan with increasing field. The data for $kd = 3\pi/4$ in Fig. 16 exhibit a second-order transition at reduced field $h_{\rm t} = 7.03$ from a helix to fan structure with increasing h_x. The second-order nature of the transition is clearly established from the field dependences of the ϕ_n in Fig. 16(a). It is also apparent from the discontinuity in $d\mu_{x\rm ave}/dh_x$ at $h_{\rm t}$ as illustrated in Fig. 16(c). For this kd, the variations of the $\phi_n(h_x)$ in the fan field range follow rather closely the prediction for the respective sinusoidal fan, as shown in Fig. 16(d).

On the other hand, the $\phi_n(h_x)$ data for $kd = 8\pi/11$ in Fig. 17(a) exhibit discontinuities with field at $h_{\rm t} = 5.46$ indicative of a first-order transition. The magnetization data in Fig. 17(b) show a small discontinuity at $h_{\rm t}$, reflecting a weak first-order transition. Expanded plots of the $\phi_n(h_x)$ in the fan region are shown in Fig. 17(c). Except for the region $h_x \to h_{\rm c}$, the data are not well described by sinusoidal fan angles as shown by the dashed black curves. A stronger first-order transition is found in the magnetization versus field for $kd = 3\pi/5$ in Fig. 18(b), where again the expanded plots of the $\phi_n(h_x)$ data in Fig. 18(c) are not well described by the sinusoidal fan model except for $h_x \to h_{\rm c}$.

Finally, Fig. 19 for $kd = 4\pi/7$ demonstrates that the behaviors of ϕ_n and $\mu_{x\rm ave}$ with field do not vary monotonically with kd. In particular, instead of first-order transitions found for the previous two kd values, the ϕ_n values now vary smoothly with h_x indicating a smooth but distinct crossover at a field $h_x = 2.57$ between the helix and fan phases as shown in Fig. 19(a). This behavior is reflected in the data for $\mu_{x\rm ave}(h_x)$ in Figs. 19(b) and 19(c). These data show that $\mu_{x\rm ave}(h_x)$ almost undergoes a first-order transition at h_x. On the other hand, the next data set for $kd = 6\pi/11$ in Fig. 20 again show smooth crossover behaviors more characteristic of the data for $kd = 10\pi/11$ to $4\pi/5$ in Figs. 12–15.

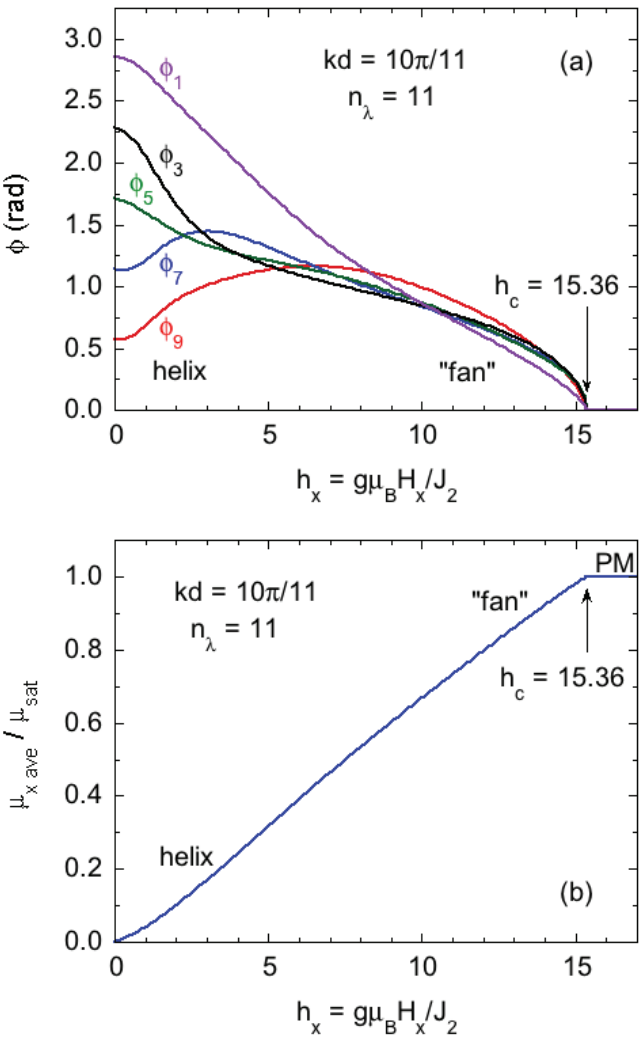

FIG. 12: (Color online) (a) The angles ϕ_9, ϕ_7, ϕ_5, ϕ_3, and ϕ_1 of the corresponding moments with respect to the $+x$ axis versus reduced in-plane field h_x for a helix with turn angle $kd = 10\pi/11$. (b) Average magnetic moment per spin in the field direction normalized by the moment magnitude, $\mu_{x\mathrm{ave}}/\mu_{\mathrm{sat}}$, versus h_x.

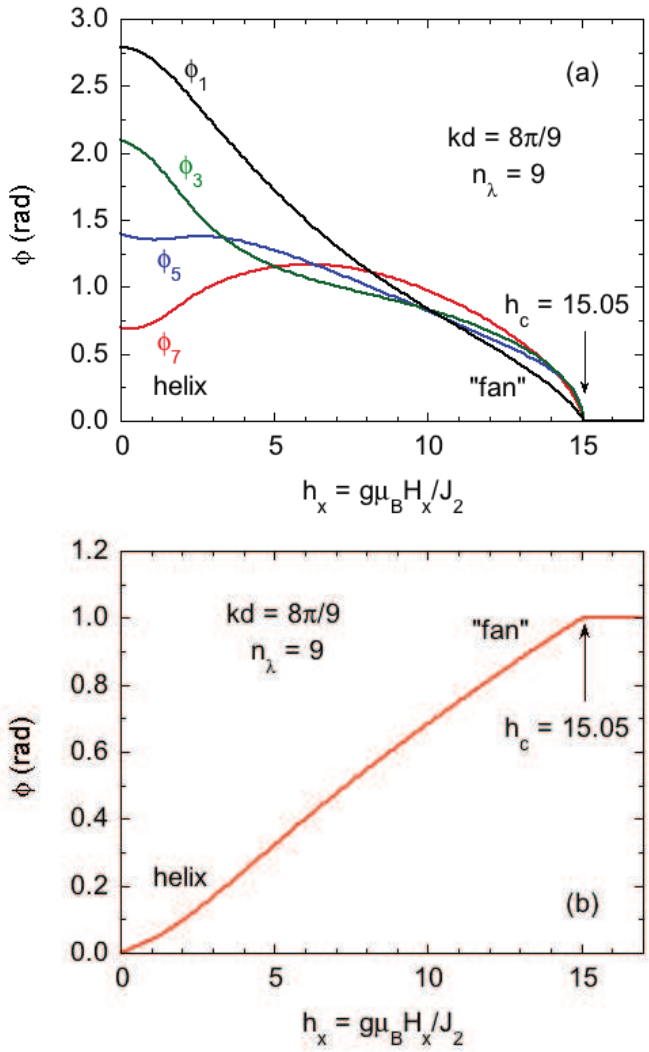

FIG. 13: (Color online) (a) The angles ϕ_7, ϕ_7, ϕ_3, and ϕ_1 of the corresponding moments with respect to the $+x$ axis versus reduced in-plane field h_x for a helix with turn angle $kd = 8\pi/9$. (b) Average magnetic moment per spin in the field direction normalized by the moment magnitude, $\mu_{x\mathrm{ave}}/\mu_{\mathrm{sat}}$, versus h_x.

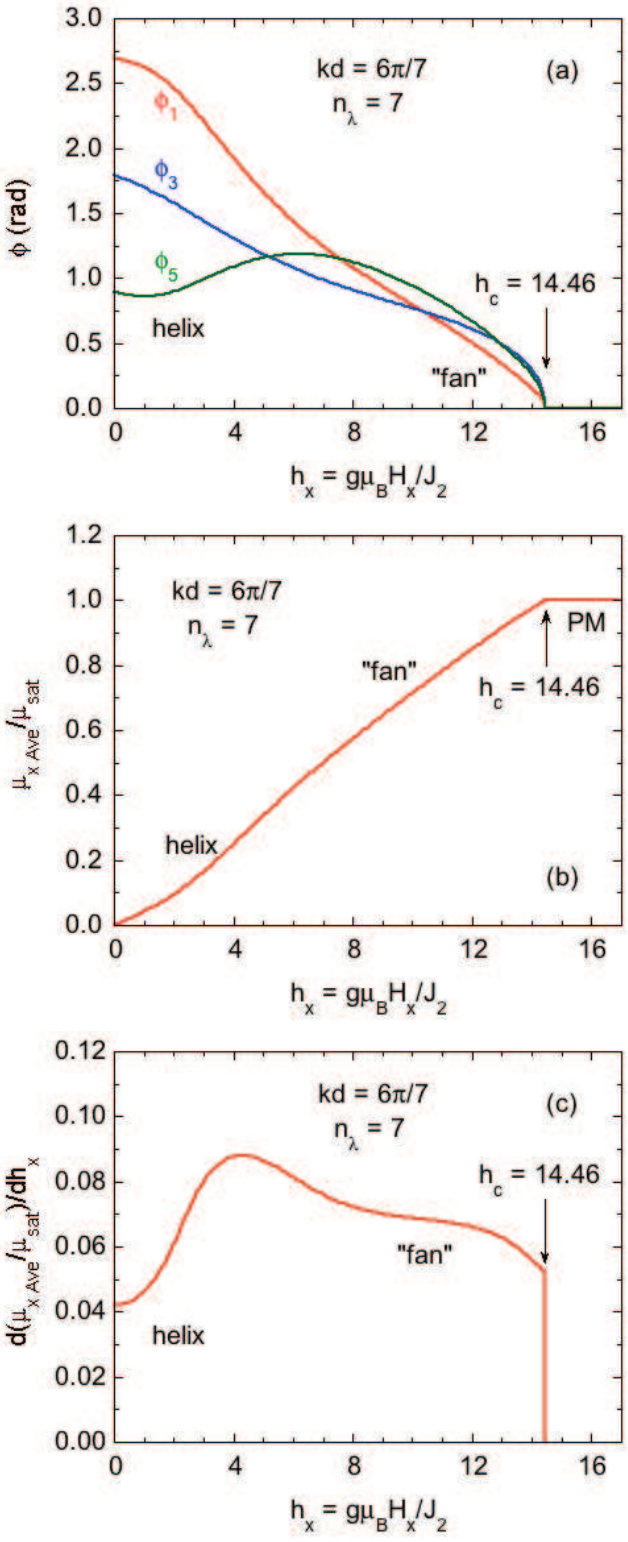

FIG. 14: (Color online) (a) The angles ϕ_5, ϕ_3, and ϕ_1 of the corresponding moments with respect to the $+x$ axis versus reduced in-plane field h_x for a helix with turn angle $kd = 6\pi/7$. (b) Average normalized magnetic moment per spin in the field direction, $\mu_{x\mathrm{ave}}/\mu$, versus h_x. (c) Derivative of the average moment in (b) with respect to h_x, exhibiting the second-order "fan" to PM phase transition at the critical field h_c.

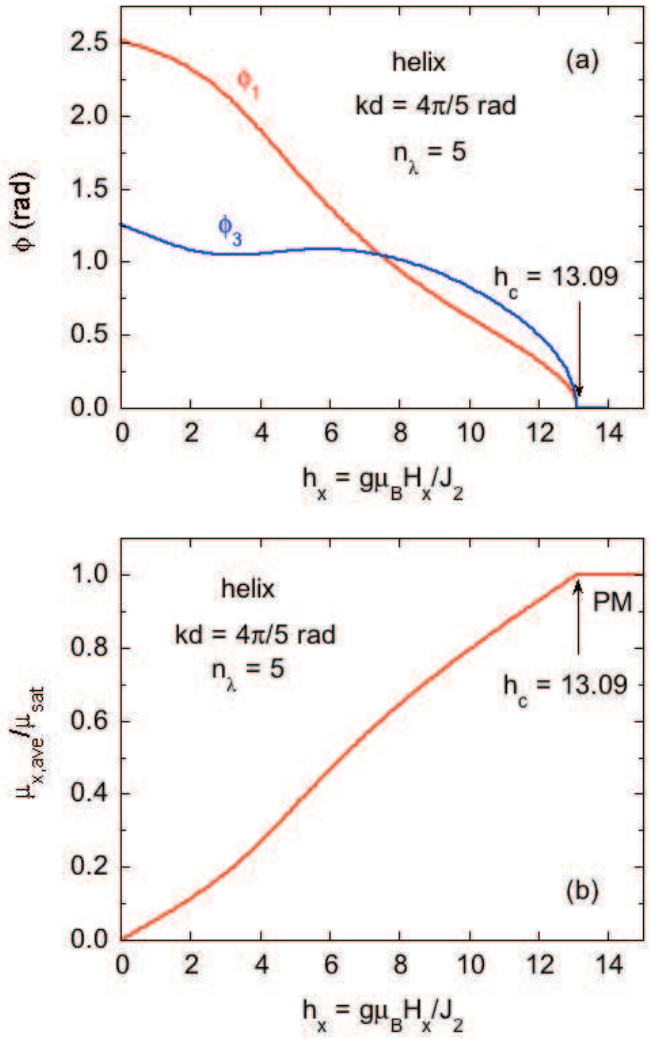

FIG. 15: (Color online) (a) The angles ϕ_3 and ϕ_1 of the corresponding moments with respect to the $+x$ axis versus reduced in-plane field h_x for a helix with turn angle $kd = 4\pi/5$. (b) Average normalized magnetic moment per spin in the field direction $\mu_{x\mathrm{ave}}/\mu$ versus h_x.

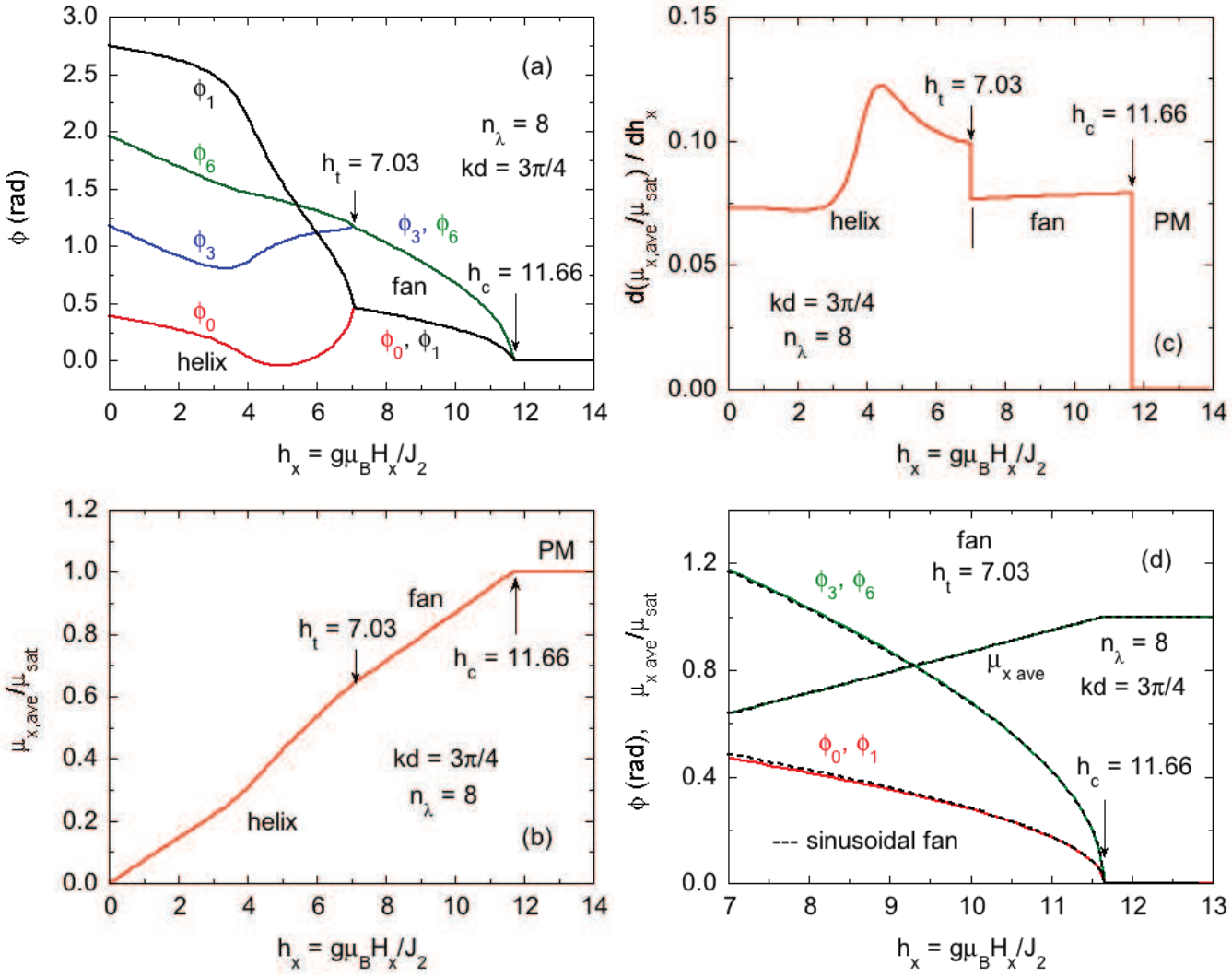

FIG. 16: (Color online) (a) The angles ϕ_0, ϕ_3, ϕ_6, and ϕ_1 of the respective moments with respect to the $+x$ axis versus reduced in-plane field h_x for a helix with turn angle $kd = 3\pi/4$. (b) Average normalized magnetic moment per spin in the field direction, $\mu_{x\mathrm{ave}}/\mu$, versus h_x. (c) Derivative of the average moment in (b) with respect to h_x. (d) Expanded plots of the ϕ_n and $\mu_{x\mathrm{ave}}/\mu$ versus h_x for the fan phase in (a) and (b), including corresponding data for the sinusoidal fan (dashed lines).

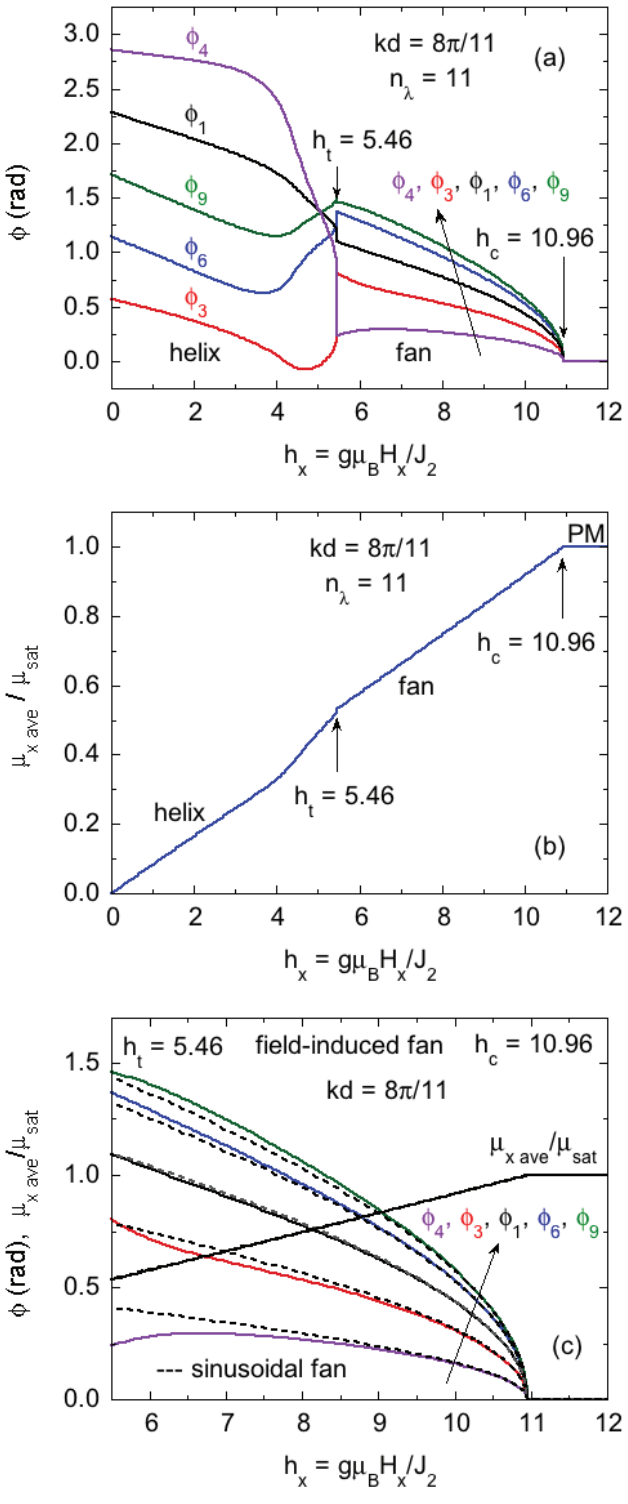

FIG. 17: (Color online) (a) The angles ϕ_3, ϕ_6, ϕ_9, ϕ_1, and ϕ_4 of the corresponding moments with respect to the $+x$ axis versus reduced in-plane field h_x for a helix with turn angle $kd = 8\pi/11$. (b) Average normalized magnetic moment per spin in the field direction, $\mu_x/\mu_{\rm sat}$, versus h_x, showing a weak first-order transition at field $h_{\rm t}$. (c) Expanded plots of the ϕ_n and $\mu_x/\mu_{\rm sat}$ in the field-induced fan range (solid lines). The predictions for a sinusoidal fan with the same kd and J_{12} are shown as black dashed lines.

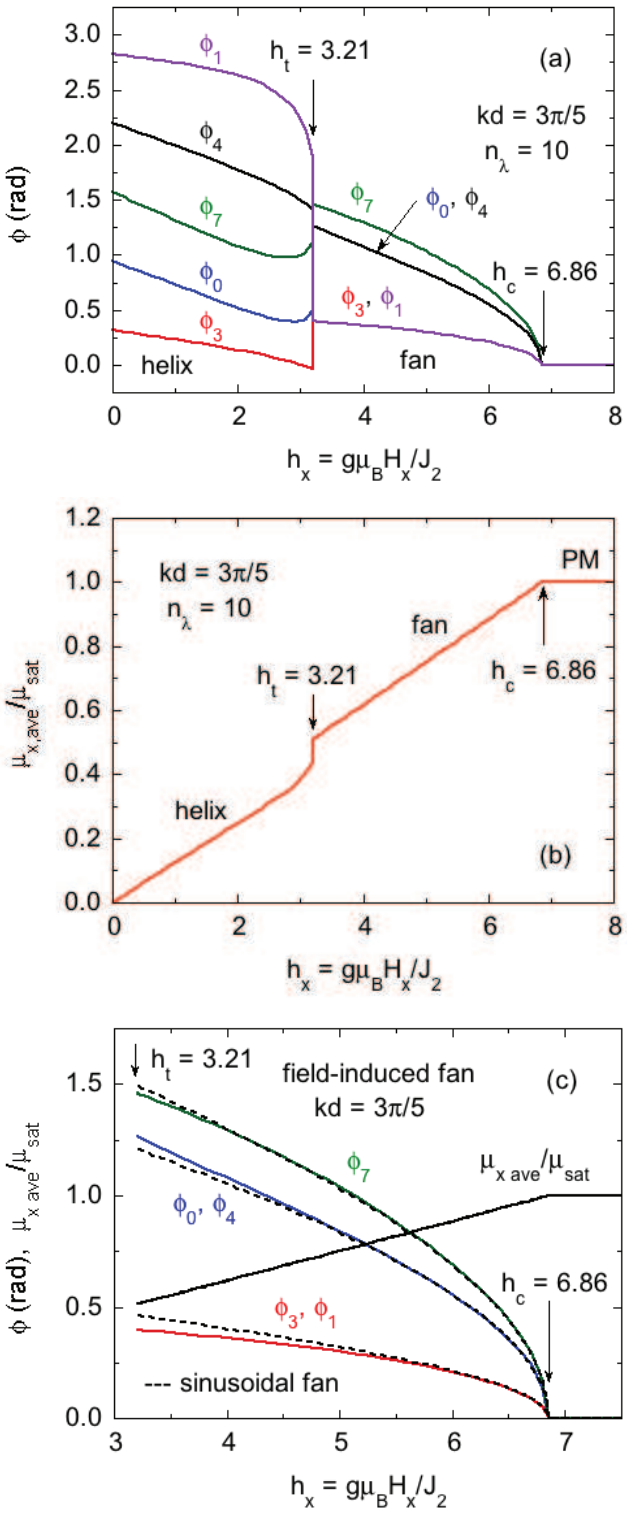

FIG. 18: (Color online) (a) The angles ϕ_3, ϕ_0, ϕ_7, ϕ_4, and ϕ_1 of the respective moments with respect to the $+x$ axis versus reduced in-plane field h_x for a helix with turn angle $kd = 3\pi/5$. (b) Average normalized magnetic moment per spin in the field direction, $\mu_{x\rm ave}/\mu_{\rm sat}$, versus h_x. (c) Expanded plots of the ϕ_n and $\mu_x/\mu_{\rm sat}$ in the field-induced fan range (solid lines). The predictions for a sinusoidal fan with the same kd and J_{12} are shown as black dashed lines.

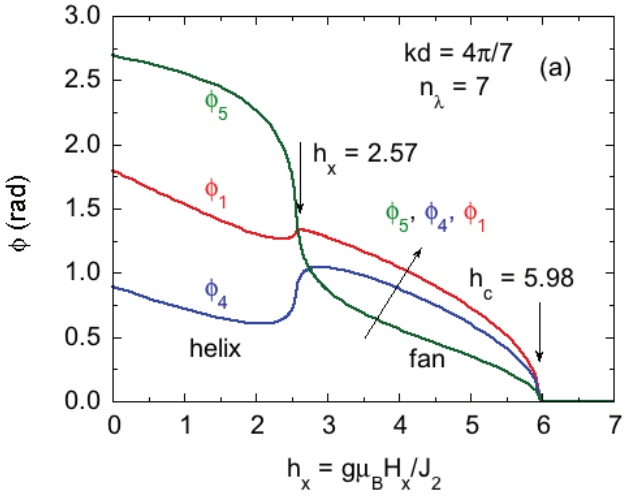

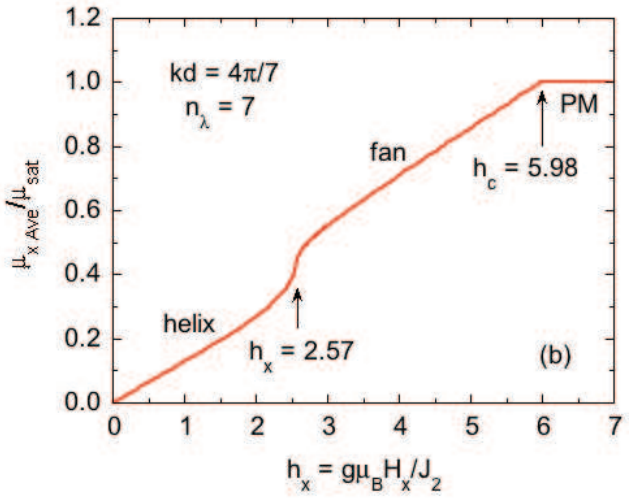

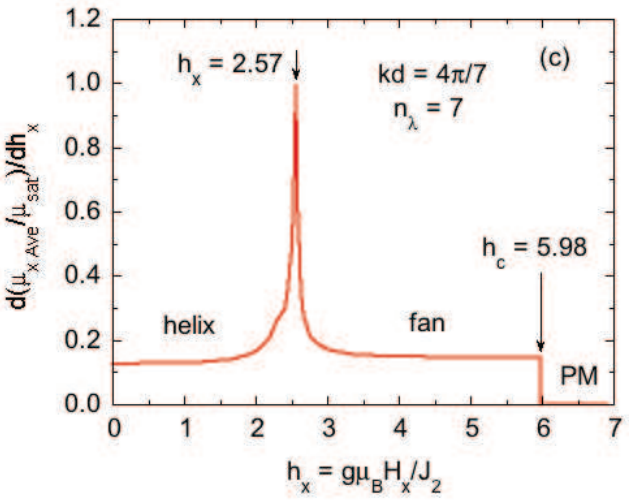

FIG. 19: (Color online) (a) The angles ϕ_4, ϕ_1, and ϕ_5 of the respective moments with respect to the $+x$ axis versus reduced in-plane field h_x for a helix with turn angle $kd = 4\pi/7$. (b) Average normalized magnetic moment per spin in the field direction, $\mu_x/\mu_{\rm sat}$, versus h_x. (c) Derivative of the average moment in (b) with respect to h_x, which shows a rapid smooth crossover between helix and fan phases at a field $h_x = 2.57$ but no phase transition.

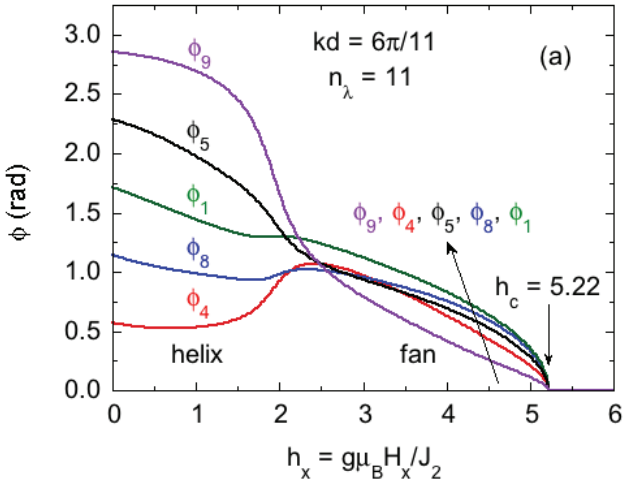

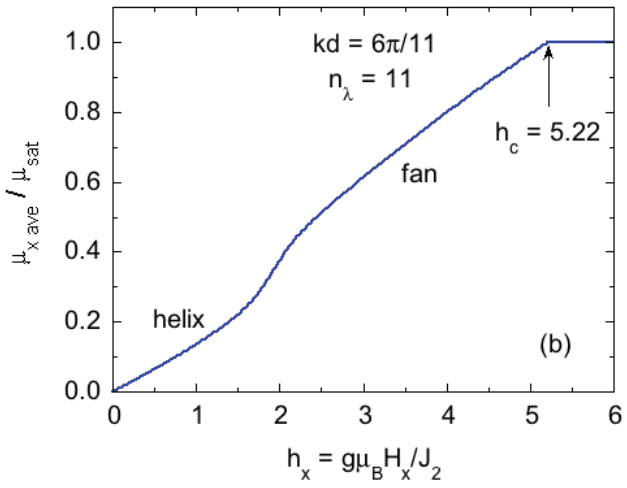

FIG. 20: (Color online) (a) The angles ϕ_4, ϕ_8, ϕ_1, ϕ_5, and ϕ_9 of the corresponding moments with respect to the $+x$ axis versus reduced in-plane field h_x for a helix with turn angle $kd = 6\pi/11$. (b) Average normalized magnetic moment per spin in the field direction, $\mu_{x\rm ave}/\mu_{\rm sat}$, versus h_x.

B. $0 < kd < \pi/2$: FM $J_1 < 0$

When moving into the regime of FM (negative) values of J_1, with decreasing kd we again find a smooth crossover between helix and fan phases as revealed for $kd = 4\pi/9$ in Fig. 21. However, this crossover results in a stronger S-shape to the $\mu_{x\mathrm{ave}}(h_x)$ data than found above in the region $\pi/2 < kd \leq \pi$, as shown in Fig. 21(b). It is clear from Fig. 21(a) that the fan angles are not sinusoidal except for $h_x \to h_\mathrm{c}$.

On the other hand, Figs. 22–30 for discrete values $kd = 2\pi/5$ to $\pi/6$ exhibit strongly first-order transitions at h_t. In all such cases, the ratio $h_\mathrm{t}/h_\mathrm{c} \sim 0.5$, even though h_c decreases by more than a factor of 20 from 1.91 to 0.0718 over this kd range. Furthermore, the $\phi_n(h_x > h_\mathrm{t})$ data are approximated by sinusoidal fans, as shown for $kd = 4\pi/11$ and $\pi/6$ in Figs. 23 and 30, respectively, where again the sinusoidal fan model is most accurate for $h_x \to h_\mathrm{c}$.

The discontinuity in $\mu_{x\mathrm{ave}}/\mu_\mathrm{sat}$ at $h_x = h_\mathrm{t}$ increases strongly with decreasing kd from 0.547 for $kd = 2\pi/5$ in Fig. 22 to 0.839 for $kd = \pi/6$ in Fig. 30. This monotonic increase in the discontinuity with decreasing kd is consistent with the value for the continuum model with $kd \to 0$ in Fig. 3, for which the discontinuity has a value of 0.875.

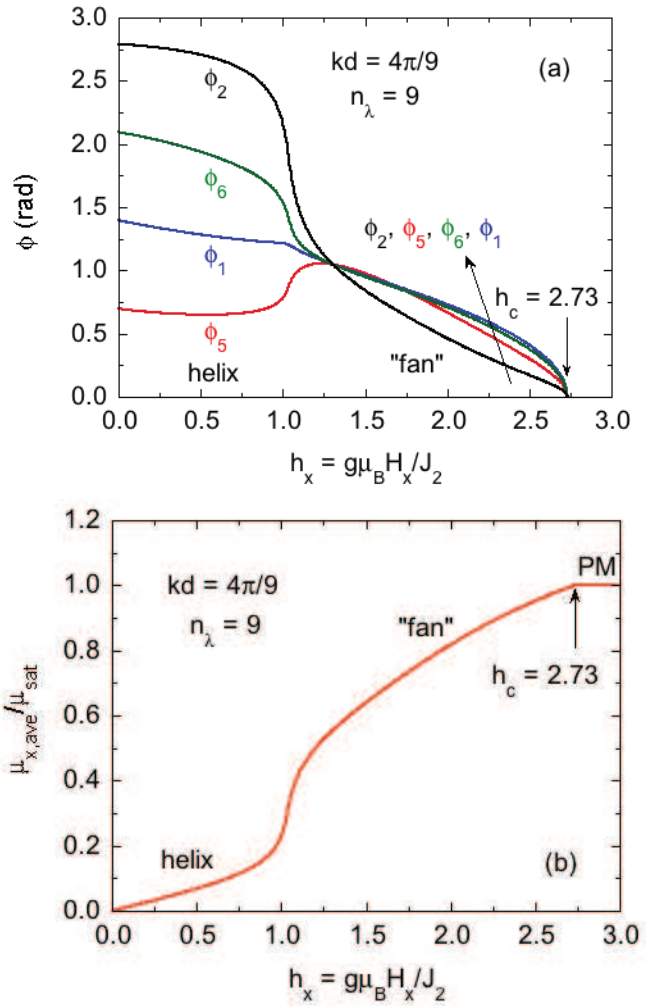

FIG. 21: (Color online) (a) The angles ϕ_5, ϕ_1, ϕ_6, and ϕ_2 of the corresponding moments with respect to the $+x$ axis versus reduced in-plane field h_x for a helix with turn angle $kd = 4\pi/9$. (b) Average normalized magnetic moment per spin in the field direction, $\mu_{x\mathrm{ave}}/\mu_\mathrm{sat}$, versus h_x.

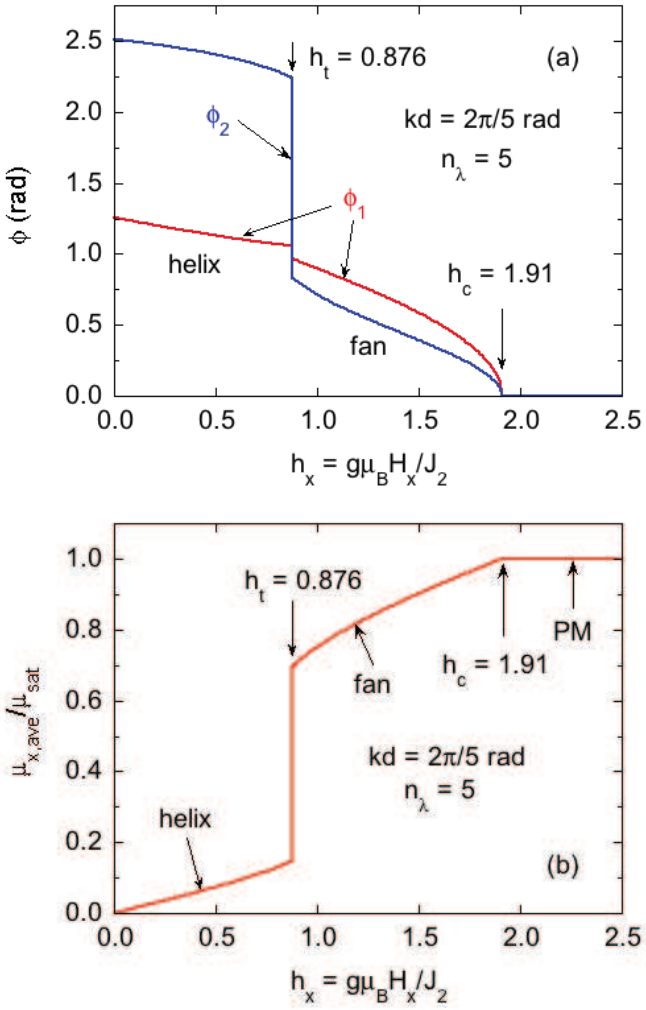

FIG. 22: (Color online) (a) The angles ϕ_1 and ϕ_2 of moments $\vec{\mu}_1$ and $\vec{\mu}_2$ with respect to the $+x$ axis versus reduced in-plane field h_x for a helix with turn angle $kd = 2\pi/5$. (b) Average normalized magnetic moment per spin in the field direction, $\mu_{x\mathrm{ave}}/\mu_{\mathrm{sat}}$, versus h_x.

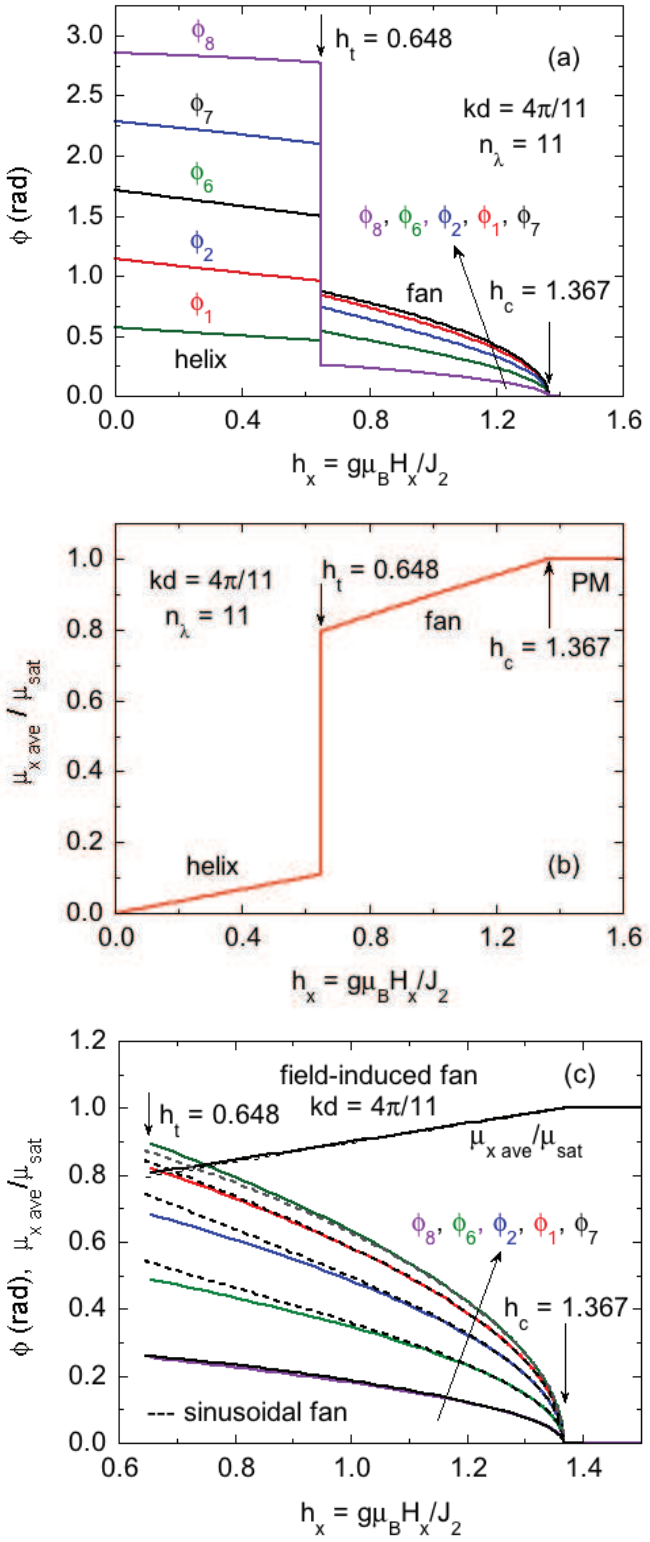

FIG. 23: (Color online) (a) The angles ϕ_1, ϕ_2, ϕ_6, ϕ_7, and ϕ_8 of the respective moments with respect to the $+x$ axis versus reduced in-plane field h_x for a helix with turn angle $kd = 4\pi/11$. (b) Average normalized magnetic moment per spin in the field direction, $\mu_{x\mathrm{ave}}/\mu_{\mathrm{sat}}$, versus reduced field h_x. (c) Expanded plots of the moment angles in (a) for the field-induced fan angles versus h_x (solid lines), together with the predictions for the corresponding sinusoidal fan (dashed lines).

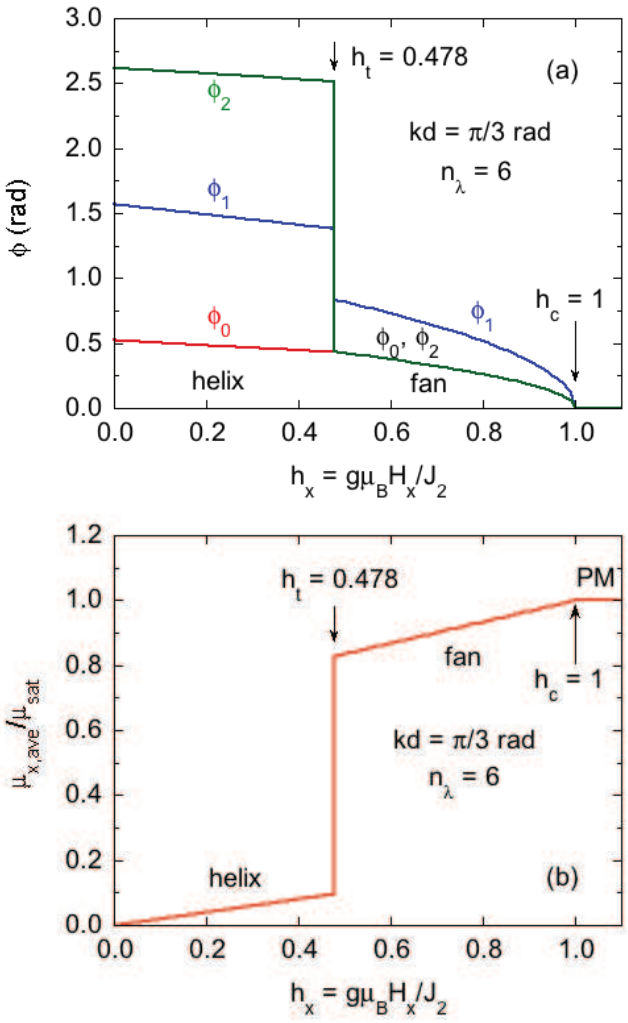

FIG. 24: (Color online) (a) The angles ϕ_0, ϕ_1, and ϕ_2 of the corresponding moments with respect to the $+x$ axis versus reduced in-plane field h_x for a helix with turn angle $kd = \pi/$. (b) Average normalized magnetic moment per spin in the field direction, $\mu_{x\mathrm{ave}}/\mu_{\mathrm{sat}}$, versus reduced field h_x.

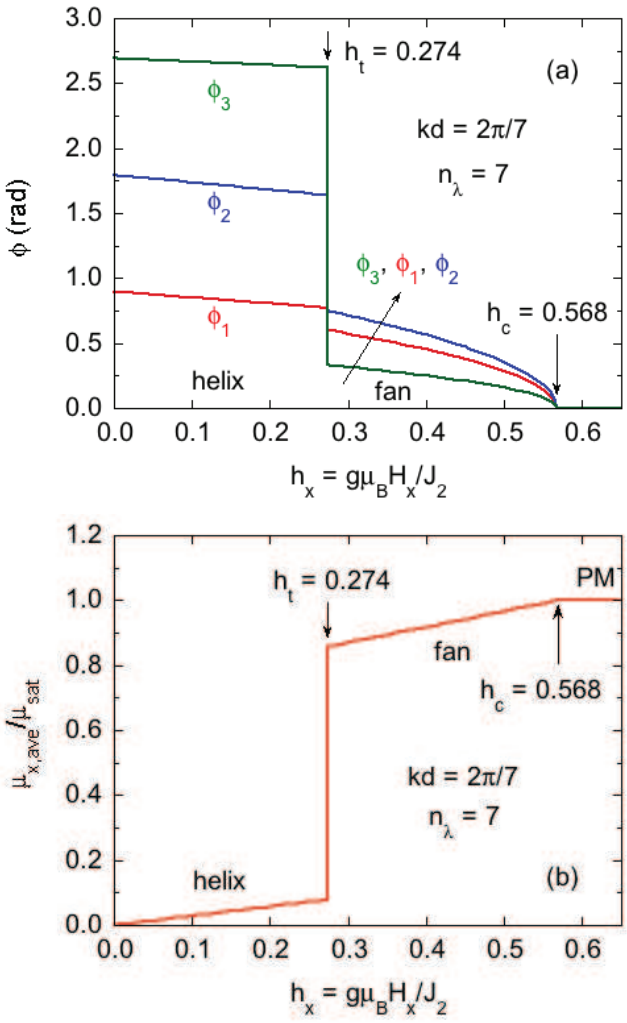

FIG. 25: (Color online) (a) The angles ϕ_0, ϕ_1, and ϕ_2 of the corresponding moments with respect to the $+x$ axis versus reduced in-plane field h_x for a helix with turn angle $kd = 2\pi/7$. (b) Average normalized magnetic moment per spin in the field direction, $\mu_{x\mathrm{ave}}/\mu_{\mathrm{sat}}$, versus reduced field h_x.

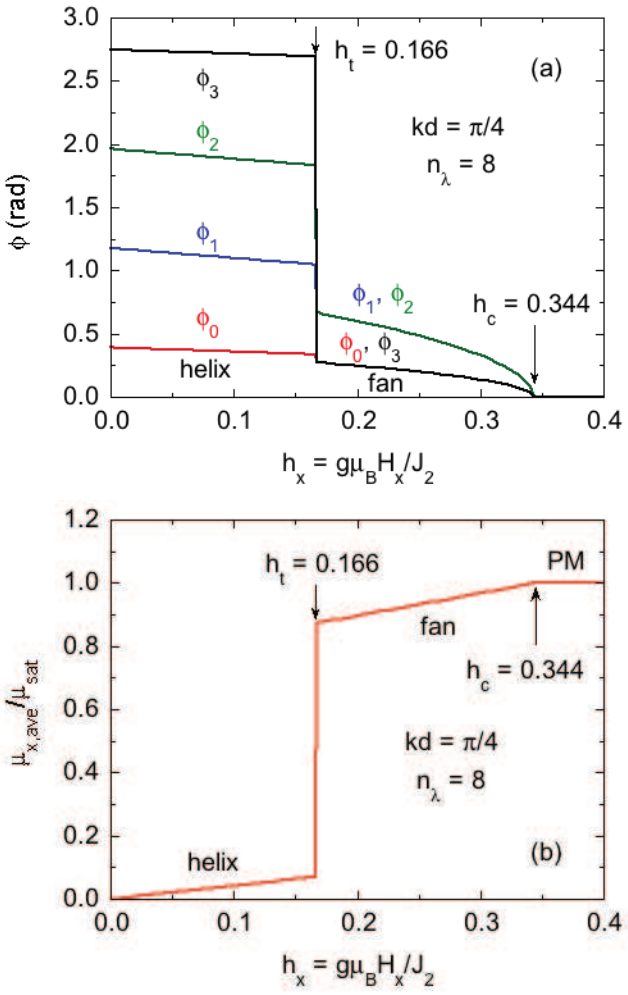

FIG. 26: (Color online) (a) The angles ϕ_0, ϕ_1, ϕ_2, and ϕ_3 of the corresponding moments with respect to the $+x$ axis versus reduced in-plane field h_x for a helix with turn angle $kd = \pi/4$. (b) Average normalized magnetic moment per spin in the field direction, $\mu_{x\mathrm{ave}}/\mu_{\mathrm{sat}}$, versus h_x.

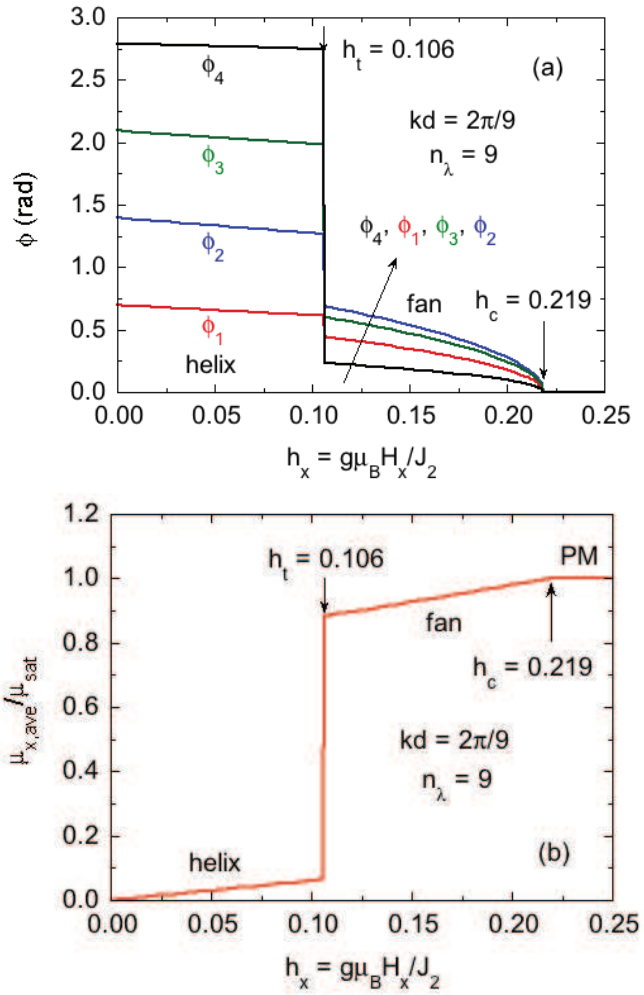

FIG. 27: (Color online) (a) The angles ϕ_1–ϕ_4 of the corresponding moments with respect to the $+x$ axis versus reduced in-plane field h_x for a helix with turn angle $kd = 2\pi/9$. (b) Average normalized magnetic moment per spin in the field direction, $\mu_{x\mathrm{ave}}/\mu_{\mathrm{sat}}$, versus h_x.

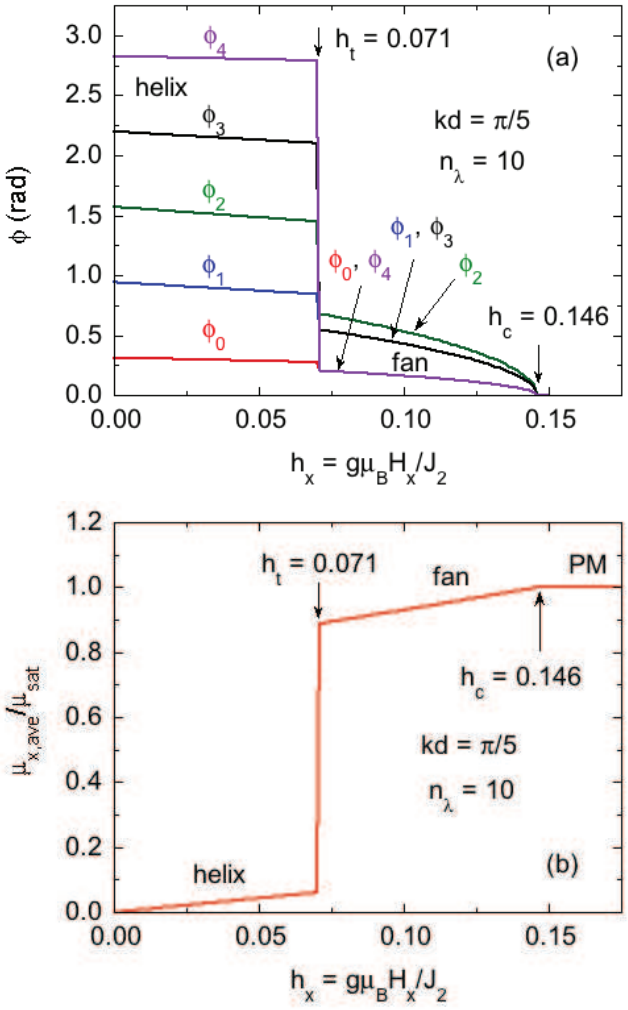

FIG. 28: (Color online) (a) The angles ϕ_0 to ϕ_4 of the corresponding moments with respect to the $+x$ axis versus reduced in-plane field h_x for a helix with turn angle $kd = \pi/5$. (b) Average normalized magnetic moment per spin in the field direction, $\mu_{x\mathrm{ave}}/\mu_{\mathrm{sat}}$, versus h_x.

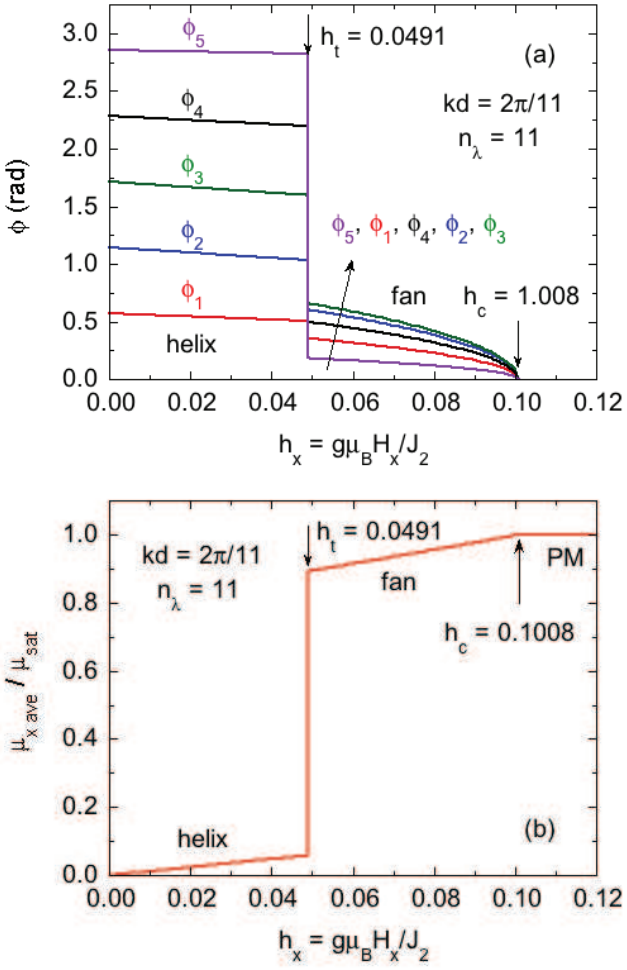

FIG. 29: (Color online) (a) The angles ϕ_1 to ϕ_5 of the correspondin moments with respect to the $+x$ axis versus reduced in-plane field h_x for a helix with turn angle $kd = 2\pi/11$. (b) Average normalized magnetic moment per spin in the field direction, $\mu_{x\mathrm{ave}}/\mu_{\mathrm{sat}}$, versus h_x.

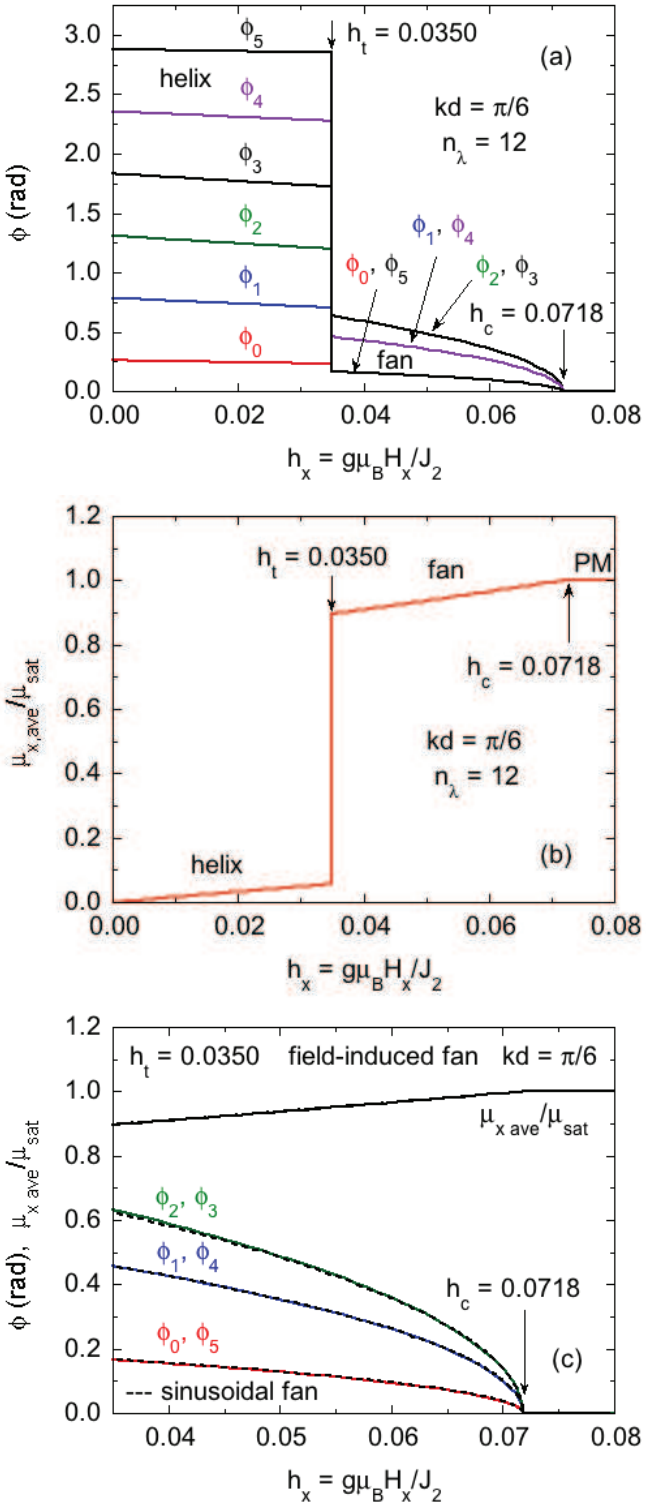

FIG. 30: (Color online) (a) The angles ϕ_0 to ϕ_5 of of the respective moments with respect to the $+x$ axis versus reduced in-plane field h_x for a helix with turn angle $kd = \pi/6$. (b) Average normalized magnetic moment per spin in the field direction, $\mu_{x\mathrm{ave}}/\mu_{\mathrm{sat}}$, versus h_x. (c) Expanded plots of the angles and average moment in the field-induced fan regime in (a) and (b) (solid lines). Also shown are the predictions for a sinusoidal fan with the same kd and J_{12} (dashed lines).

V. SUMMARY OF HELIX DATA WITH FIXED TURN ANGLE kd

A summary of our data for the helix phase and helix to fan transitions where kd is independent of field for the full range $0 < kd \leq \pi$ is given in Table IV. The data include the first- or second-order (as noted) reduced transition field $h_{\rm t}$ and the critical field $h_{\rm c}$ at which the normalized average magnetization per spin $\mu_{x\rm ave}/\mu_{\rm sat}$ saturates to the value of unity obtained from energy minimization. If the data for a given value of kd exhibit only a crossover from helix to fan with increasing h_x, the $h_{\rm t}$ column entry reads "none". Also included for each value of kd in the table are the critical field for the sinusoidal fan by itself obtained from Eqs. (21), the ratio $h_{\rm t}/h_{\rm c}$, and the initial reduced susceptibility $\chi_x(h_x \to 0) \equiv \mu_{x\rm ave}/h_x$ of the helix.

Table IV shows that $h_{\rm c}$ determined from energy minimization, where the ϕ_n were free to vary independently to obtain the minimum energy, and the value $h_{\rm c\,Fan}$ for the sinusoidal fan with the same kd and J_{12} given by the value $J_{12} = -4\cos(kd)$ for the helix, are identical. This indicates that the field-induced fan structure of the helix approaches a sinusoidal fan with the same kd and J_{12} for $h_x \to h_{\rm c}$, as previously inferred [7].

From the data in Table IV, one sees that χ_x increases rapidly with decreasing kd. For the limit $kd \to 0$, Enz predicted [12]

$$\chi_x = \frac{1}{10(kd)^4}. \tag{28a}$$

For the series $kd = 2\pi/n_\lambda$, one obtains

$$\chi_x = \frac{n_\lambda^4}{10(2\pi)^4} \approx 6.416 \times 10^{-5} n_\lambda^4. \tag{28b}$$

Plotted in Fig. 31(a) are the values of χ_x/n_λ^4 versus n_λ from the data in Table IV for the series $kd = 2\pi/n_\lambda$ with $n_\lambda = 5$ to 12. Also shown as the horizontal dashed line is the continuum limit for $n_\lambda \to \infty$ given by Eq. (28b). One sees that the continuum limit $n_\lambda \to \infty$ is already approached within $\sim 20\%$ by $n_\lambda = 12$.

Enz also made a prediction that the $kd \to 0$ limit of the ratio $h_{\rm t}/h_{\rm c}$ is

$$\frac{h_{\rm t}}{h_{\rm c}} = 1/2. \tag{28c}$$

The ratios $h_{\rm t}/h_{\rm c}$ from Table IV are plotted in Fig. 31(b) versus n_λ, again for the series $kd = 2\pi/n_\lambda$, and are seen to fairly closely approach the continuum limit of 1/2 (horizontal dashed line) with increasing n_λ even by $n_\lambda = 12$.

The zero-temperature phase diagram obtained from the data in Table IV is shown in Fig. 32, where the 11 first-order transitions and the single second-order transition are indicated by filled squares and a filled circle, respectively. It apears that the region $0 < kd \leq 2\pi/5$ forms a continuum of phases where the helix phase undergoes

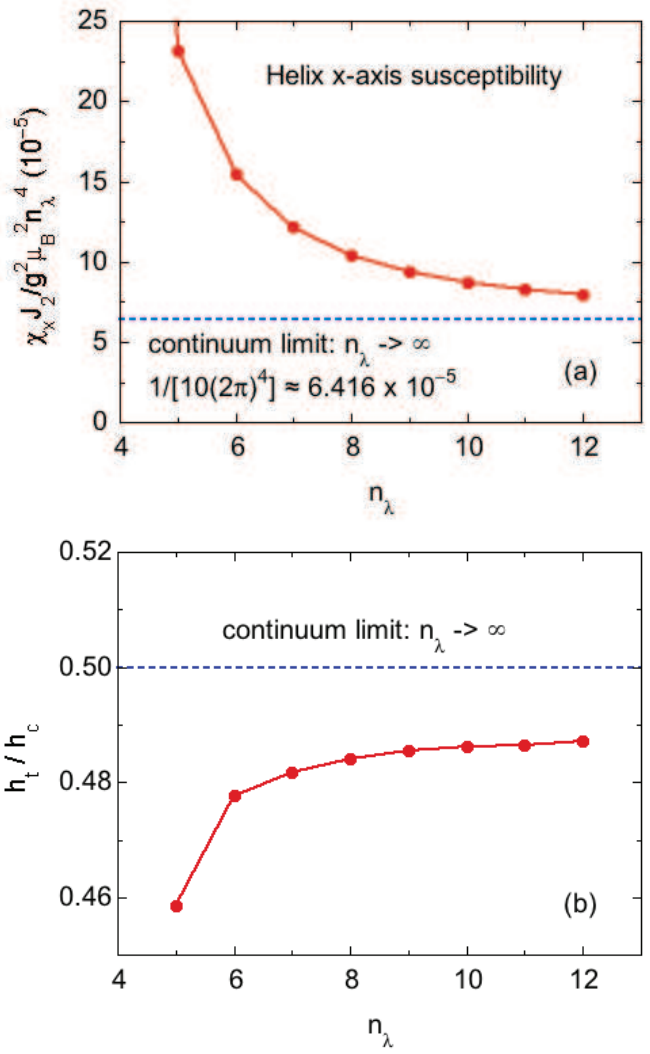

FIG. 31: (Color online) (a) Normalized magnetic susceptibility per spin $\chi_x J_2/g^2\mu_{\rm B}^2$ divided by n_λ^4, where n_λ is the number of layers per helix wavelength and the angle between the ordered moments in successive layers of the helix along the z axis is $2\pi/n_\lambda$. (b) The ratio of the first-order helix to fan transition field $h_{\rm t}$ and the fan to paramagnet critical field $h_{\rm c}$. The horizontal blue dashed lines in (a) and (b) are the respective $n_\lambda \to \infty$ continuum limits in Eqs. (28) [12].

a first-order transition to a fan phase at a reduced field $h_{\rm t}/h_{\rm c}$ that smoothly increases with decreasing kd, reaching the continuum limit of 1/2 in Eq. (28c) for $kd \to 0$. On the other hand, the first and second-order transitions for $3\pi/5 \leq kd \leq 3\pi/4$ are nestled between kd values that show continuous crossovers between the helix and fan phases, and further surprises may be in store if additional rational values of kd are explored in the range $4\pi/9 < kd < 1$.

TABLE IV: Phase transition fields for the helix to fan ($h_{\rm t}$) if present, and helix or fan to the paramagnetic phase ($h_{\rm c}$), obtained by minimizing the energy of the helix or field-induced fan. The critical field for the fan phase with J_{12} set to the value for the helix, taken from the exact data in Table III and Eqs. (21), are listed as $h_{\rm c\,Fan}$. Also shown are the initial reduced susceptibilities of the helix phase $\chi_x \equiv \mu_{x\rm ave}/h_x$. Exact solutions are given if obtained. "N/A" means "not applicable".

kd	kd/π	n_λ	$h_{\rm t}$ (helix $\to$ fan)	$h_{\rm c}$ (helix/fan)	$h_{\rm c\,Fan}$ (helix J_{12})	$h_{\rm t}/h_{\rm c}$	$\chi_x(h_x \to 0)$ (helix)
π	1	2	none	16	16	N/A	$1/16 = 0.0625$
$10\pi/11$	0.909091	11	none	15.359	15.3585	N/A	0.0352993
$8\pi/9$	0.888889	9	none	15.050	15.0496	N/A	0.0374703
$6\pi/7$	0.857143	7	none	14.455	14.4547	N/A	0.0421042
$5\pi/6$	0.833333	12	none	13.929	13.9282	N/A	$(11-6\sqrt{3})/13 \approx 0.0467458$
$4\pi/5$	0.8	5	none	13.091	13.0902	N/A	$(1-1/\sqrt{5})/10 \approx 0.0552786$
$3\pi/4$	0.75	8	7.028^a	11.657	11.6569	0.6029	$(1-1/\sqrt{2})/4 \approx 0.0732233$
$8\pi/11$	0.727273	11	5.459^b	10.955	10.9543	0.4983	0.0832981
$2\pi/3$	0.666667	3	none	9	9	N/A	$1/9 \approx 0.111111$
$3\pi/5$	0.6	10	3.205^b	6.860	6.85410	0.4672	$(3-\sqrt{5})/6 \approx 0.127322$
$4\pi/7$	0.571429	7	none	5.979	5.97823	N/A	0.127887
$6\pi/11$	0.545455	11	none	5.220	5.21953	N/A	0.126732
$\pi/2$	0.5	4	N/A	N/A	4	N/A	N/A
$4\pi/9$	0.444444	9	none	2.732	2.73143	N/A	0.130047
$2\pi/5$	0.4	5	0.8758^b	1.910	1.90983	0.4585	$(1+1/\sqrt{5})/10 \approx 0.144721$
$4\pi/11$	0.363636	11	0.6475^b	1.367	1.36696	0.4737	0.168098
$\pi/3$	0.333333	6	0.4777^b	1	1	0.4777	$1/5 = 0.2$
$2\pi/7$	0.285714	7	0.2732^b	0.5671	0.567040	0.4818	0.291547
$\pi/4$	0.25	8	0.1661^b	0.3432	0.343146	0.4840	$(1+1/\sqrt{2})/4 \approx 0.426777$
$2\pi/9$	0.222222	9	0.1063^b	0.2190	0.218941	0.4854	0.616267
$\pi/5$	0.2	10	0.0710^b	0.1460	0.145898	0.4863	$(3+\sqrt{5})/6 \approx 0.872678$
$2\pi/11$	0.181818	11	0.04905^b	0.10081	0.100802	0.4866	1.210426
$\pi/6$	0.166667	12	0.03497^b	0.07180	0.0717968	0.4870	$(11+6\sqrt{3})/13 \approx 1.645562$
0^+	0^+	∞	0^+	0^+	0^+	1/2 [12]	∞ [12]

[a] Second-order transition
[b] First-order transition

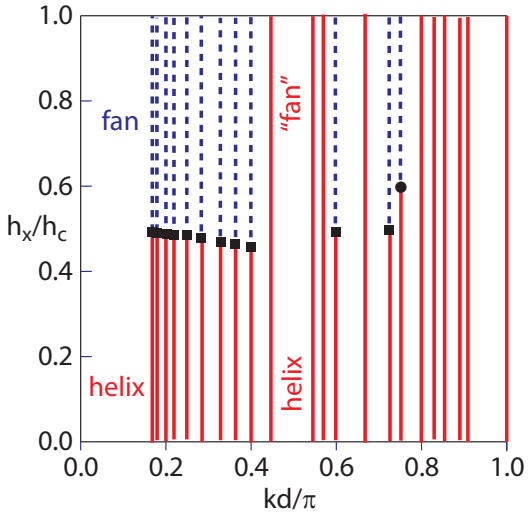

FIG. 32: (Color online) Reduced magnetic field h_x/h_c versus normalized turn angle kd/π phase diagram determined from the data in Table IV. The red solid vertical lines represent the field stability range of the (distorted) helix structure, whereas the vertical dashed blue lines represent the fan phase which can be approximated by a sinusoidal fan phase. Field-induced first-order transitions are denoted by filled squares. The single second-order transition is denoted by a filled circle. The helix to "fan" notation denotes a continuous evolution from the helix to a fanlike structure that is quite different from a sinusoidal fan. The structures and properties of the helix and fan are indistinguishable for each of $kd/\pi = 2/3$ and 1.

Acknowledgments

The author is grateful for collaboration and discussions about $EuCo_2P_2$ with N. S. Sangeetha. This work was supported by the U.S. Department of Energy, Office of Basic Energy Sciences, Division of Materials Sciences and Engineering. Ames Laboratory is operated for the U.S. Department of Energy by Iowa State University under Contract No. DE-AC02-07CH11358.

[1] D. C. Johnston, Magnetic Susceptibility of Collinear and Noncollinear Heisenberg Antiferromagnets, Phys. Rev. Lett. **109**, 077201 (2012).

[2] D. C. Johnston, Unified molecular field theory for collinear and noncollinear Heisenberg antiferromagnets, Phys. Rev. B **91**, 064427 (2015).

[3] For extensive comparisons of the unified MFT with experimental data, see D. C. Johnston, Unified Molecular Field Theory for Collinear and Noncollinear Heisenberg Antiferromagnets, arXiv:1407.6353v1.

[4] N. S. Sangeetha, E. Cuervo-Reyes, A. Pandey, and D. C. Johnston, $EuCo_2P_2$: A model molecular-field helical Heisenberg antiferromagnet, Phys. Rev. B. **94**, 014422 (2016).

[5] D. C. Johnston, Magnetic dipole interactions in crystals, Phys. Rev. B **93**, 014421 (2016).

[6] D. C. Johnston, Influence of uniaxial single-ion anisotropy on the magnetic and thermal properties of Heisenberg antiferromagnets within unified molecular field theory, Phys. Rev. B **95**, 094421 (2017).

[7] T. Nagamiya, K. Nagata, and Y. Kitano, Magnetization Process of a Screw Spin System, Prog. Theor. Phys. **27**, 1253 (1962).

[8] Y. Kitano and T. Nagamiya, Magnetization Process of a Screw Spin System. II, Prog. Theor. Phys. **31**, 1 (1964).

[9] T. Nagamiya, Helical Spin Ordering — Theory of Helical Spin Configurations, *Solid State Physics*, Vol. 20, edited by F. Seitz, D. Turnbull, and H. Ehrenreich (Academic Press, New York, 1967), pp. 305–411.

[10] J. M. Robinson and P. Erdös, Behavior of Helical Spin Structures in Applied Magnetic Fields, Phys. Rev. B **2**, 2642 (1970).

[11] B. Carazza, E. Rastelli, and A. Tassi, Planar spin chain with competing interactions in an external magnetic field, Z. Phys. B **84** 301 (1991).

[12] U. Enz, Magnetization Process of a Helical Spin Configuration, J. Appl. Phys. Suppl. **32**, 22S (1961).

[13] A. Beléndez, C. Pascual, D. I. Méndez, and C. Neipp, Exact solution for the nonlinear pendulum, Rev. Brasil. Ensino Física. **29**, 645 (2007).

[14] F. M. S. Lima, Analytical study of the critical behavior of the nonlinear pendulum, Am. J. Phys. **78**, 1146 (2010).

[15] M. Reehuis, W. Jeitschko, M. H. Möller, and P. J. Brown, A Neutron Diffraction Study of the Magnetic Structure of $EuCo_2P_2$, J. Phys. Chem. Solids **53**, 687 (1992).